Evolving dunes under flow reversals: from an initial heap toward an inverted dune

Willian Righi Assis[1], Erick Franklin[1], and Nathalie Vriend[2]

[1]UNICAMP - University of Campinas
[2]University of Colorado Boulder

July 20, 2023

Abstract

Sand dunes are ubiquitous in nature, and are found in abundance on Earth and other planetary environments. One of the most common types are crescent-shaped dunes known as barchans, whose mid-line could be assumed to behave as 2D dunes. In this work, we (i) compare the morphology of the mid-line of 3D barchans with 2D dunes; and (ii) track the evolution of 3D barchan and 2D dunes under bi-modal changes in the flow direction. We performed experiments in a 2D flume on 2D dunes and Euler-Lagrange simulations of 3D bedforms. The reversal experiments start with an initial heap deforming into a steady-state dune, which is then perturbed by reversing the flow, resulting in an inverted dune. We show that during the reversal the grains on the lee side immediately climb back onto the dune while its internal part and toe remain static, forming a new lee face on the previous stoss slope of varying angle. We determine that (i) the characteristic time for the development of 2D dunes scales identically with that for 3D barchans, (ii) that the time for dune reversal is twice the time necessary to develop an initial heap to steady-state, and (iii) that a considerable part of grains remain static during the entire process. Our findings reveal the mechanisms for dune reversal, and highlight that numerical computations of 2D barchans, which are more feasible in geophysical scales, predict realistic outcomes for the relevant time-scales.

Evolving dunes under flow reversals: from an initial heap toward an inverted dune

W. R. Assis[1], E. M. Franklin[1], N. M. Vriend[2,3,4,5]

[1]School of Mechanical Engineering, UNICAMP - University of Campinas, Rua Mendeleyev, 200, Campinas, SP, Brazil
[2]BP Institute, University of Cambridge, Cambridge, UK
[3]Department of Applied Mathematics and Theoretical Physics, University of Cambridge, Cambridge, UK
[4]Department of Earth Sciences, University of Cambridge, Cambridge, UK
[5]Current address: Department of Mechanical Engineering, University of Colorado Boulder, Boulder, USA

Key Points:

- Experiments show that 2D dunes grow and develop over a characteristic time that matches that of fully 3D barchan dunes
- The morphodynamics of reversing dunes over time are revealed by fully reversing the flow direction and tracking the rebuilding and reshaping
- Numerical simulations on a reversing 3D barchan show that its central slice behaves as the reversing 2D dunes

Corresponding author: Willian Assis, righiassis@gmail.com

Abstract

Sand dunes are ubiquitous in nature, and are found in abundance on Earth and other planetary environments. One of the most common types are crescent-shaped dunes known as barchans, whose mid-line could be assumed to behave as 2D dunes. In this work, we (i) compare the morphology of the mid-line of 3D barchans with 2D dunes; and (ii) track the evolution of 3D barchan and 2D dunes under bi-modal changes in the flow direction. We performed experiments in a 2D flume on 2D dunes and Euler-Lagrange simulations of 3D bedforms. The reversal experiments start with an initial heap deforming into a steady-state dune, which is then perturbed by reversing the flow, resulting in an inverted dune. We show that during the reversal the grains on the lee side immediately climb back onto the dune while its internal part and toe remain static, forming a new lee face on the previous stoss slope of varying angle. We determine that (i) the characteristic time for the development of 2D dunes scales identically with that for 3D barchans, (ii) that the time for dune reversal is twice the time necessary to develop an initial heap to steady-state, and (iii) that a considerable part of grains remain static during the entire process. Our findings reveal the mechanisms for dune reversal, and highlight that numerical computations of 2D barchans, which are more feasible in geophysical scales, predict realistic outcomes for the relevant time-scales.

Plain Language Summary

Crescent-shaped dunes, known as barchans, are found in abundance on Earth and other planetary environments. Although their different shapes and manifestations intrigue us and produce fascinating images, the underlying physics still challenges us. Here we investigate two critical questions: (i) can we capture all relevant physical processes of 3D dunes in a 2D slice? and (ii) how does the dune morph over space and time upon flow reversal (e.g. the wind blowing from the opposite direction)? We research these questions by carrying out experiments with 2D dunes in a water flume and numerical simulations of 3D barchans, and flip-around our flow forcing to investigate flow reversal. We find that the typical development times for 2D and 3D dunes are equivalent and reveal details of the rebuilding processes of the dune upon flow reversals. Interestingly, the inversion time after flow reversal is twice that of the formation time of the initial heap, and a considerable part of grains remains static during the entire process. Our findings reveal the mechanisms for dune reversal and show that 2D simulations, which are simpler and faster, reproduce the underlying physics.

1 Introduction

Sand dunes are bedforms resulting from erosion and deposition of sand by the action of a fluid flow (Bagnold, 1941; Hersen et al., 2002), and they are frequently found on Earth, Mars and other celestial bodies (Hersen, 2004; Elbelrhiti et al., 2005; Claudin & Andreotti, 2006; Parteli & Herrmann, 2007; Courrech du Pont, 2015). Among the most common are crescent-shaped dunes, known as barchans, that appear under an one-directional flow regime and when the quantity of available sand is limited.

Given the abundance of barchans present in nature, a considerable number of field measurements, experiments, and numerical simulations were conducted over the last decades (C. Sauermann et al., 2000; Hersen et al., 2002; Andreotti et al., 2002; Hersen et al., 2004; Hersen, 2004; Kroy et al., 2005, 2002b; Parteli et al., 2007; Andreotti et al., 2009; Franklin & Charru, 2011; Pähtz et al., 2013; Kidanemariam & Uhlmann, 2014; Guignier et al., 2013; Parteli et al., 2011; Khosronejad & Sotiropoulos, 2017), but only very few of them were carried out at the grain scale (Alvarez & Franklin, 2018, 2019, 2020, 2021; Assis & Franklin, 2020, 2021). Most analytical models and numerical simulations are based on information from field measurements on aeolian dunes, so that they solve the problem at the bedform scale only by considering that the grains move mainly in the longitudinal direction (typical of aeolian saltation). For example, the first numerical simulations considered the granular system as a continuum medium, some of them modeling 3D dunes as vertical slices that behave as 2D dunes. Those models hypothesize that grains move in the longitudinal direction, while transverse diffusion transfers a small quantity of mass between adjoining slices (G. Sauermann et al., 2001; Herrmann & Sauermann, 2000; Kroy et al., 2002a, 2002b, 2005; Schwämmle & Herrmann, 2005; Parteli et al., 2014). Therefore, the continuum-sliced models are, in principle, valid for aeolian barchans, which consist of a large number of grains that are entrained mainly in longitudinal direction, with small lateral motion (due to reptation). However, this is not necessarily the case of subaqueous barchans where transverse sediment transport can become dominant.

Some recent works showed that the transverse motion of grains is important for subaqueous barchans (Alvarez & Franklin, 2018, 2019), indicating that the picture of a 3D dune as connected slices must be refined in the subaqueous case. For instance, Alvarez and Franklin (2018, 2019) measured experimentally the displacement of individual grains migrating to horns as an initial pile was deformed into a barchan dune. They found that most of those grains come from upstream regions on the periphery of the dune, within angles forming 105° and 160° and 210° and 260° in the flow direction (0° pointing downstream). Those results were later corroborated by numerical simulations at the grain scale using large eddy simulation coupled with discrete element method (LES-DEM, Alvarez & Franklin, 2020, 2021; Lima et al., 2022). In this picture, grains migrating to horns have considerable transverse displacements (of the order of the dune size), contradicting, for subaqueous barchans, the models based on connected slices. Note however that the results show that grains going to horns do not come from the dune centerline.

Based on discrete simulations using a cellular automaton model, Zhang et al. (2014) found that the residence time of grains within a barchan dune, in particular in the central slice, is relatively large, being of the order of many turnover times of the barchan. They showed that the large residence time occurs because of a cyclic process: grains on the stoss side tend to disperse toward the laterals (as also shown by the experiments of Assis & Franklin, 2021), but are returned to the central region after avalanching on the lee side due to the curvature of the barchan dune. On the whole, Zhang et al. (2014) showed that transverse mixing in the central slice is restricted by this dispersion-concentration mechanism, and proposed that the central slice contains most of the information (and memory) of the barchan morphodynamics. This result is not, in principle, in contradiction with those of Alvarez and Franklin (2018, 2019), since the latter found that grains populating the horns (and afterward leaving the barchan) do not come from the central slice.

Because the interior (e.g, the central slice) of real dunes is not accessible in experiments, Bacik et al. (2020); Bacik, Caulfield, and Vriend (2021); Bacik, Canizares, et al. (2021) carried out experiments with 2D dunes in a narrow Couette-type circular water flume. Bacik et al. (2020) investigated how 2D dunes interact with each other under a turbulent water flow, and found that the turbulent structures of the flow trigger a long range dune-dune repulsion (preventing dune-dune collisions). Later Bacik, Caulfield, and Vriend (2021), inquired into the stability of a pair of dunes and proposed a parameter space where dune-dune interactions either stabilize or destabilize the initial configuration, and Bacik, Canizares, et al. (2021) showed how the presence of obstacles change the dune morphodynamics. If these findings can be proven valid for barchan dunes, they would represent a large advance toward understanding barchan fields.

Our aim is to investigate whether subaqueous 3D barchan dunes can be represented as connected slices, in essence as the 2D dune as introduced in Bacik et al. (2020); Bacik, Caulfield, and Vriend (2021); Bacik, Canizares, et al. (2021), or whether indeed the transverse sediment transport radically changes the physical behavior and needs to be accounted for. In addition, we are investigating whether the underlying physical processes of dune reversal leading to an inverted dune can be captured as a solely 2D process mimicking the mid-line of a 3D barchan dune. We are performing experiments in the 2D flume on heaps and reversing dunes and complement these experiments with numerical simulations at the grain-scale, which allows us to analyze the central slice of 3D dunes. In our numerical simulations, we apply the same forcing procedure as in our experiments: (1) pile formation, (2) development to a steady-state dune, (3) flow reversal and (4) equilibrating to a steady-state (reversed) dune. As the grains climb back up the lee side during the flow reversal stage, the internal part and the toe of the dune remain static while a new lee face with varying angle and length is formed on the former stoss slope. In this manuscript, we will identify characteristic times and scales of this reversal process, and identify the areas where the grains are remobilized in this re-morphing process. Our findings reveal the mechanisms for dune reversal and provide a validation between experimental data and numerical simulations.

2 Experimental Setup

The experimental setup is the same as used in Jarvis et al. (2022); Bacik et al. (2020), and consists of a periodic channel, a driving device, and an imaging system. The periodic channel is a circular flume with external and internal radii of 97 cm and 88 cm, respectively, filled to a level of 45.5 cm with water and particles, with parameters specified in the next paragraph. A rotating rig with 12 equidistant paddles submerged near the water surface is mounted above the flume, providing a shearing motion to the water, while the flume is connected to a counter-rotating turntable. Our tests begin by imposing a paddle rotation in the counter-clockwise direction (view from above) and a turntable rotation in the clockwise direction (we call this flow 0°). After reaching a steady-state developed dune, we revert both the paddle and turntable directions in order to obtain a reverse flow (180°). Figures 1a and 1b show a photograph and the layout of the experimental setup, respectively.

We used round glass spheres (ρ_s = 2500 kg/m^3, approximately), sieved to a diameter between 1.0 mm $\leq d \leq$ 1.3 mm, for which we consider the mean value as being $\bar{d}$ = 1.15 mm, and varied the total mass of the initial pile between 1 and 2 kg (see the supporting information for a photograph of the used particles). The flow direction was either 0° (initial flow) or 180° (reverse flow), and the water velocity varied within 0.81 m/s $\leq U \leq$ 1.22 m/s. In here, the relative velocity between the table and paddles is $U = R(\Omega_p - \Omega_t)$, the outer radius is R = 97 cm, and Ω_p and Ω_t are the angular velocities of the paddles and table, respectively. The shear velocity u_* is computed based on Equation 8 of Jarvis et al. (2022), and was found to vary between 0.050 m/s $\leq u_* \leq$ 0.103 m/s. The Reynolds number $Re = Uw/\nu$ varied within 0.73 × 10^5 and 1.10 × 10^5, where w = 9 cm is the width of the channel and ν the kinematic viscosity of water. The paddle and water heights were fixed for all tests, being 34.5 and 45.5 cm, respectively. Table 1 summarizes the test conditions, and images from experiments are available in an open repository (Assis et al., 2023). For a given velocity U, the exact angular velocities Ω_p and Ω_t were chosen empirically to reduce secondary flows in order to produce 2D dunes as symmetrical as possible (lateral-view images from 2D dunes are available in the supporting information).

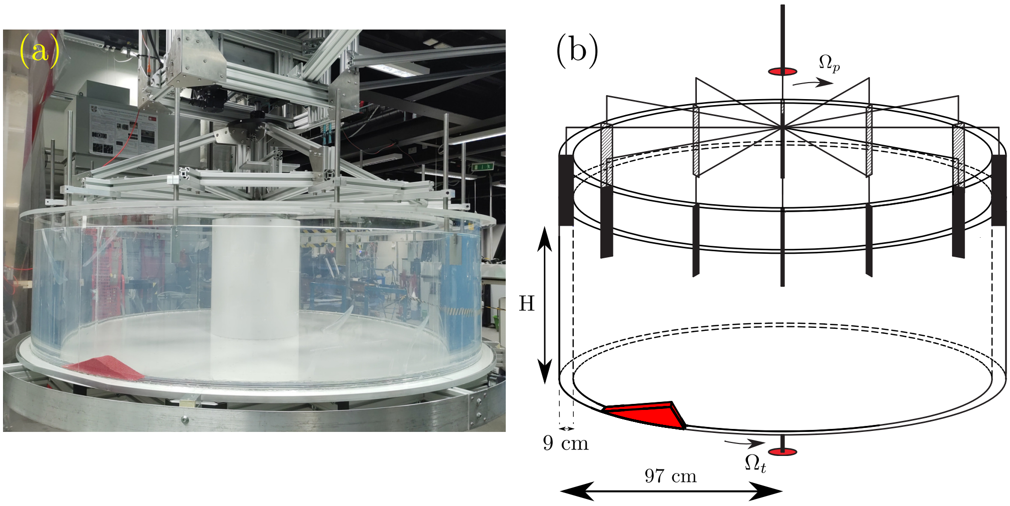

Figure 1. (a) Photograph and (b) Layout of the circular flume.

Case ···	Dune mass kg	Ω_p rpm	Ω_t rpm	Ω_p - Ω_t rpm	Re ···	Flow direction degrees
a	2	4.60	-3.40	8	0.73×10^5	0
b	2	5.80	-4.20	10	0.91×10^5	0
c	2	7.00	-5.00	12	1.10×10^5	0
d	1	4.60	-3.40	8	0.73×10^5	0
e	1	5.65	-4.35	10	0.91×10^5	0
f	1	6.85	-5.15	12	1.10×10^5	0
g	2	-4.60	3.40	-8	0.73×10^5	180
h	2	-5.80	4.20	-10	0.91×10^5	180
i	2	-7.00	5.00	-12	1.10×10^5	180
j	1	-4.60	3.40	-8	0.73×10^5	180
k	1	-5.65	4.35	-10	0.91×10^5	180
l	1	-6.85	5.15	-12	1.10×10^5	180

Table 1. Label of tested cases, dune mass, angular velocity of paddles, angular velocity of the table, total angular velocity, channel Reynolds number Re, and flow orientation.

A camera of complementary metal-oxide-semiconductor (CMOS) type was mounted with a lateral view (i.e., in the radial direction) of the flume. We used a ISVI black and white camera, capable of acquiring images at a maximum resolution of 12MP at 181 Hz (model IC-X12S-CXP), and a Nikon lens of 60 mm focal distance and F2.8 maximum aperture (model AF Micro Nikkor). In the experiments, we set the camera to operate with a region of interest (ROI) of 64 px × 1,024 px at a frequency of 200 Hz. The field of view was 6.6 mm × 105.5 mm, corresponding to a resolution of 9.7 px/mm. A column in the central axis of the rotating experiment (see Figure 1) was illuminated with lamps of light-emitting diode (LED), enabling a good contrast between the sediment layers and walls. The acquired images were afterward processed by numerical scripts that identify and reconstruct 2D profiles providing a dune shape.

3 Numerical Setup

We carried out numerical simulations using CFD-DEM (computational fluid dynamics - discrete element method), in which we computed the formation of single barchans from initially conical piles and, after reaching a developed barchan shape, reversed the flow direction. Our simulations were performed at the grain scale by making use of LES (large eddy simulation) for CFD, which thus computed the mass (Equation 1) and momentum (Equation 2) equations for the fluid using meshes of the order of the grains' diameter,

$$\nabla \cdot \vec{u}_f = 0\,, \tag{1}$$

$$\frac{\partial \rho_f \vec{u}_f}{\partial t} + \nabla \cdot (\rho_f \vec{u}_f \vec{u}_f) = -\nabla P + \nabla \cdot \vec{\vec{\tau}} + \rho_f \vec{g} - \vec{f}_{fp}\,, \tag{2}$$

where $\vec{g}$ is the acceleration of gravity, $\vec{u}_f$ is the fluid velocity, ρ_f is the fluid density, P the fluid pressure, $\vec{\vec{\tau}}$ the deviatoric stress tensor of the fluid, and $\vec{f}_{fp}$ is the resultant of fluid forces acting on each grain by unit of fluid volume. The DEM solved the linear (Equation 3) and angular (Equation 4) momentum equations applied to each solid particle,

$$m_p \frac{d\vec{u}_p}{dt} = \vec{F}_p\,, \tag{3}$$

$$I_p \frac{d\vec{\omega}_p}{dt} = \vec{T}_c\,, \tag{4}$$

where, for each grain, m_p is the mass, $\vec{u}_p$ is the velocity, I_p is the moment of inertia, $\vec{\omega}_p$ is the angular velocity, $\vec{T}_c$ is the resultant of contact torques between solids, and $\vec{F}_p$ is the resultant force (weight, contact and fluid forces). We made use of the open-source code CFDEM (Goniva et al., 2012) (www.cfdem.com), which couples the open-source CFD code OpenFOAM with the open-source DEM code LIGGGHTS (Kloss & Goniva, 2010; Berger et al., 2015). A complete description of the fundamental and implemented equations, CFD meshes and convergence, DEM parameters, and tests can be found in Lima et al. (2022).

The CFD domain is a 3D channel of size L_x = 0.4 m, $L_y = \delta$ = 0.025 m and L_z = 0.1 m, where x, y and z are the longitudinal, vertical and spanwise directions, respectively, with periodic conditions in the longitudinal and spanwise directions. The vertical dimension of the domain, $L_y = \delta$, corresponds to the channel half height (the real channel height being 2δ), and the height of smallest meshes (close to the bottom boundary) was $\Delta y = 2.9 \times 10^{-4}$ m, which corresponds to $\Delta y/d = 1.46$ (the values of d used in the simulations are shown next). The fluid is water, flowing with a cross-sectional mean velocity U = 0.28 m/s. The channel Reynolds number based on U, Re $= U2\delta\nu^{-1}$, is 14,000, and the Reynolds number based on shear velocity u_*, Re$_* = u_*\delta\nu^{-1}$, is 400, where ν is the kinematic viscosity (10^{-6} m^2/s for water). The granular material consisted of 10^5 glass spheres randomly distributed, with sizes following a Gaussian distribution within

0.15 mm $\leq d \leq$ 0.25 mm. The coefficients of sliding friction μ, rolling friction μ_r and restitution e, as well as the values of Poisson ratio σ, Young's modulus E and density ρ_p used in the simulations are shown in Table 2 (extensive tests of these parameters are presented in Lima et al., 2022). We selected for the particles a solid wall boundary condition at the bottom boundary, and a free exit at the outlet. Note that no influx of grains was imposed, so that the bedform lose grains and decrease slightly in size along time. We note also that the numerical setup differs from the experimental one in terms of fluid flow, grain diameter, boundary conditions, and size of the system. While, on the one hand, to simulate barchans with a size comparable to the 2D experiments would be computationally unfeasible, on the other hand the numerical setup used has been extensively investigated and validated against experiments (Lima et al., 2022). In addition, the use of periodic conditions for the grains (to be closer to the experimental setup) would imply that grains leaving the two horns would return and reach regions close to the flanks of the barchan dune, deforming it considerably. More details about the equations, parameters and meshes used in the simulations can be found in Lima et al. (2022).

Table 2. Physical properties of DEM particles.

DEM properties	
Sliding Friction Coeff. μ	0.6
Rolling Friction Coeff. μ_r	0.00
Restitution Coef. e	0.1
Poisson Ratio σ	0.45
Young's Modulus E (MPa)	5
Density ρ_p (kg/m^3)	2500

The first step was to simulate a pure fluid (in the absence of solid particles) flowing in the periodic channel until reaching fully-developed turbulence, and store the output to be used as initial condition in the CFD-DEM simulations (which are periodic only for the fluid). This step aimed at obtaining the initial conditions for the fluid with relatively low computational cost. Then, prior to each simulation, the grains are allowed to fall freely in stationary water, forming a conical heap in the channel center. Finally, the CFD-DEM simulations begin by imposing a turbulent water flow (whose initial condition was the previously stored fully-turbulent flow), which deforms the conical pile into a barchan dune. When a developed barchan is achieved, the flow is stopped and its direction reversed. Files with the setups used in our CFD-DEM simulations are available in an open repository (Assis et al., 2023).

4 Results and Discussion

4.1 Development of a dune from an initial heap

For the experiments outlined in cases a to f (Table 1), we followed the bedform as it evolves from an initial heap into a 2D dune. For example, Figure 2 shows reconstructed snapshots of an initial pile being deformed into a 2D dune for case c. We initially observe the elongation of the upstream side and the formation of an avalanche face downstream of the crest, with the corresponding decrease of the crest height. Afterward, from a certain time on (76 s in this case), the dune keeps roughly the same shape, indicating a developed state. On the right, Figure 2 shows the superposition of the side view of the initial (t = 4 s, in darker gray) and developed (t = 76 s, in lighter gray) dunes. Because the intersected area (in black) is proportional to the number of grains that did not move (not necessarily equal, though), it indicates that a considerable part of the dune remains static, and that the dune reaches its developed form prior to a complete turnover.

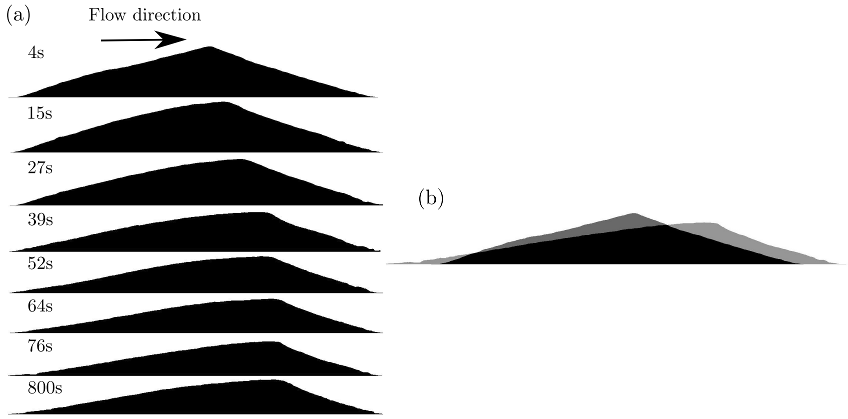

Figure 2. (a) Snapshots showing lateral-view images of an initial heap being deformed into a 2D dune for case *c* (Table 1). The flow is from left to right in the images, and the corresponding time instants are shown on the left. (b) Superposition of the side view of the initial ($t = 4$ s, in darker gray) and developed ($t = 76$ s, in lighter gray) bedforms (intersection appears in black).

In order to investigate further the dune development, we measured the main morphological scales (length L, height Z and slope θ) along time.

Figures 3a–f present the vertical position of the maximum height (crest) of bedforms, Z, as a function of time, t, for cases a to f, respectively. In this figure, Z is normalized by the dune length in the streamwise direction, L, and time t_c which is a timescale for the growth of subaqueous barchans proposed by Alvarez and Franklin (2017),

$$t_c = \frac{L_{eq}(\rho_p/\rho)(\rho_p/\rho - 1)gd}{(u_*^2 - u_{th}^2)^{3/2}} \ , \tag{5}$$

where u_{th} is shear velocity at the threshold for the incipient motion of grains, L_{eq} is the length of the developed dune, and $g = |\vec{g}|$. Because t_c in Equation 5 is proportional to L_{eq} divided by the dune celerity (displacement velocity of the dune crest), it scales with the dune turnover time. In Equation 5, we computed the threshold velocity in accordance with Andreotti et al. (2002).

For all cases, we observe in Figure 3 the existence of two timescales: a fast timescale occurring for $t/t_c < 5$, where Z/L decreases relatively fast, and a slow one for $t/t_c > 10$, where Z/L remains constant or oscillates around a mean value (plateau). While the fast timescale represents the flattening of the initial heap being deformed into a dune, the slow timescale indicates the presence of a developed dune. Therefore, the intersection between those two scales corresponds to the typical time for the formation of a 2D dune from an initial heap, for which we find $t/t_c \approx 5$. This value is higher, but of the same order of magnitude, of that found by Alvarez and Franklin (2017) for the development of barchan dunes based on the growth of their horns: $t/t_c \approx 2.5$. Because the mechanisms of barchan formation are different from those of 2D dunes, which do not have horns, this proximity of typical times is a strong indication of the existence of a similitude between the 2D dunes and the central slice of barchans. In order to inquire further into it, we performed three-dimensional CFD-DEM simulations of an initial pile being deformed into a barchan dune by a water flow, and analyze next the behavior of its central slice. Figure 4 shows snapshots of the central slice of a barchan dune (width equal to 2 mm, i.e., $10d$ for different instants (see the supporting information for snapshots showing top view images of the barchan dune, and a movie showing the time evolution of the

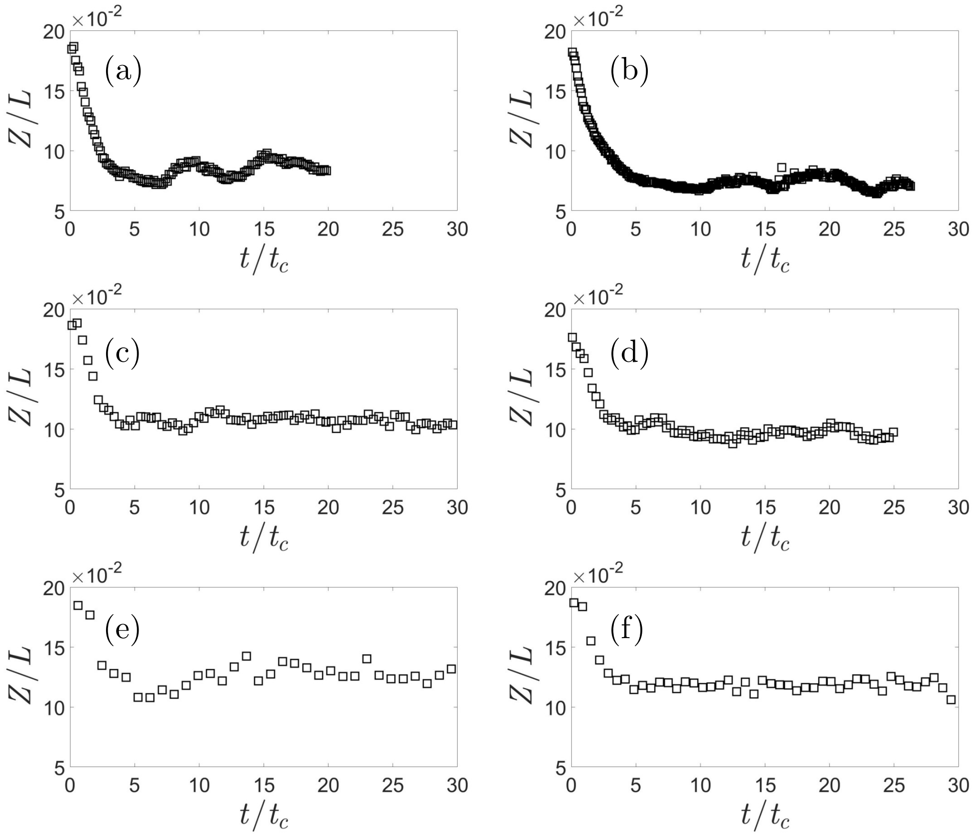

Figure 3. Vertical position of the maximum height (crest) of bedforms Z normalized by the dune length L, as a function of time t normalized by the timescale t_c. Figures (a), (c), (e) and (b), (d), (f) correspond to cases d, e, f and a, b, c (Table 1), respectively.

central slice). This width was chosen to avoid excessive fluctuations (due to the lack of grains in the spanwise direction) while analyzing the central slice only. Figures showing the longitudinal distribution of the slope, $\theta(x)$, for different time instants are available in the supporting information, for both the experiments and numerical simulations (central slice). They present a similar trend, with slightly higher mean values of $\theta(x)$ for the experiment.

In our simulations, the central slice had a much smaller number of grains than the 2D dunes, which was imposed by the computational costs of the CFD-DEM simulations (we limited the total number of grains in order to keep simulation times small). Even with this size difference, we observe that Figure 4 shows a behavior similar to that of Figure 2, with an elongation of the upstream side and formation of an avalanche face on the lee side, until a stable shape is reached (after 85 s. See figure S10 in the supporting information for the superposition of the central slice of the numerical dune). Figure 5a shows the time evolution of the horn length L_h, normalized by the characteristic length L_{drag}, as the conical pile is deformed into a barchan dune. In Figures 5a and 5b, L_h is computed as the average of the two horns, and $L_{drag} = (\rho_p/\rho_f)\, d$ is an inertial length, proportional to the flux saturation length (Hersen et al., 2002). We observe an increase in L_h along time, until a plateau is reached at $t/t_c \approx$ 1–1.5, with L_h oscillating around a mean value. The origin of oscillations are probably the small number of particles and

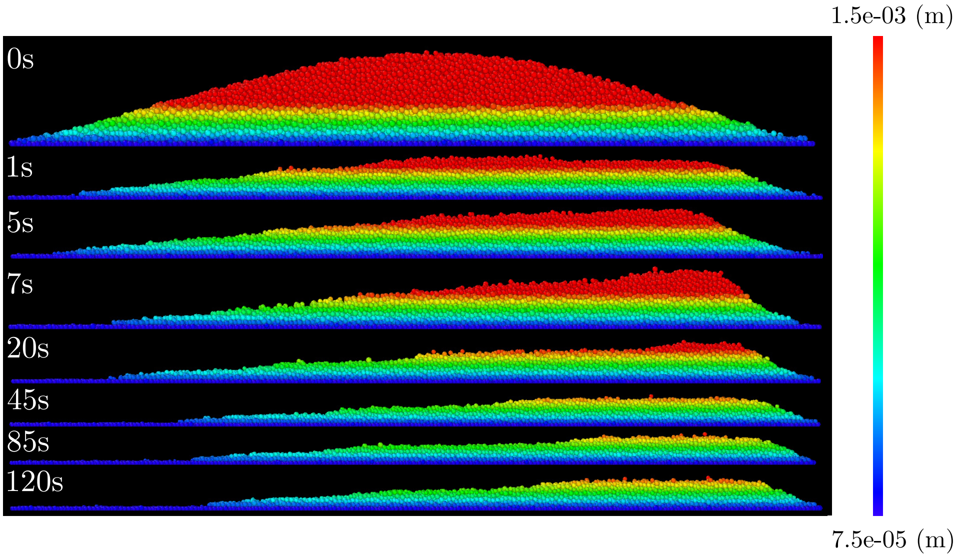

Figure 4. Snapshots showing the central slice of a bedform being deformed into a barchan dune. The water flow is from left to right and the color represents the height (scale in the colorbar on the right). The corresponding time instants are shown on the left.

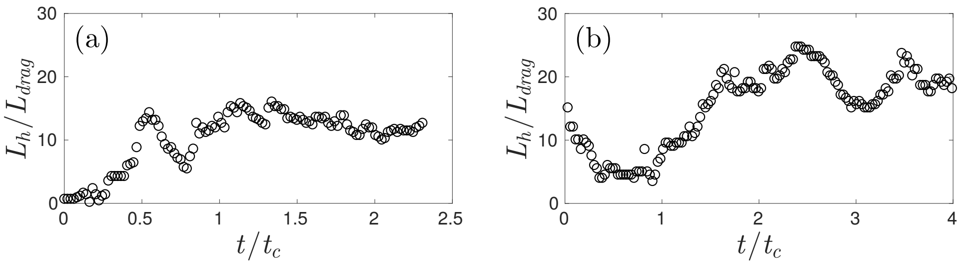

Figure 5. Time evolution of the horn length L_{horn} normalized by the characteristic length L_{drag} for (a) a barchan developed from a conical pile, and (b) for a barchan undergoing flow reversal. Results from numerical simulations, and the time is normalized by t_c.

the intermittent motion of grains. For this very small barchan, the time to reach the plateau is of the same order as that obtained experimentally by Alvarez and Franklin (2017).

In summary, by comparing the formation of 2D dunes with that of barchans from an initial heap (triangular in two and conical in three dimensions), we observe a certain similarity between them, the central slice of the barchan dune behaving roughly as a 2D dune.

4.2 Flow reversal

We inquire now into the process of inverting a dune by reversing the water flow. To create this condition, we performed experiments and numerical simulations in which we reversed the water flow after assuring that the dune was in a steady-state developed state. For the experiments with 2D dunes, this corresponds to cases g to l of Table 1. Figure 6 shows reconstructed snapshots of an initially developed 2D dune undergoing a flow reversal (case h). We notice that initially the motion occurs over the previous avalanche

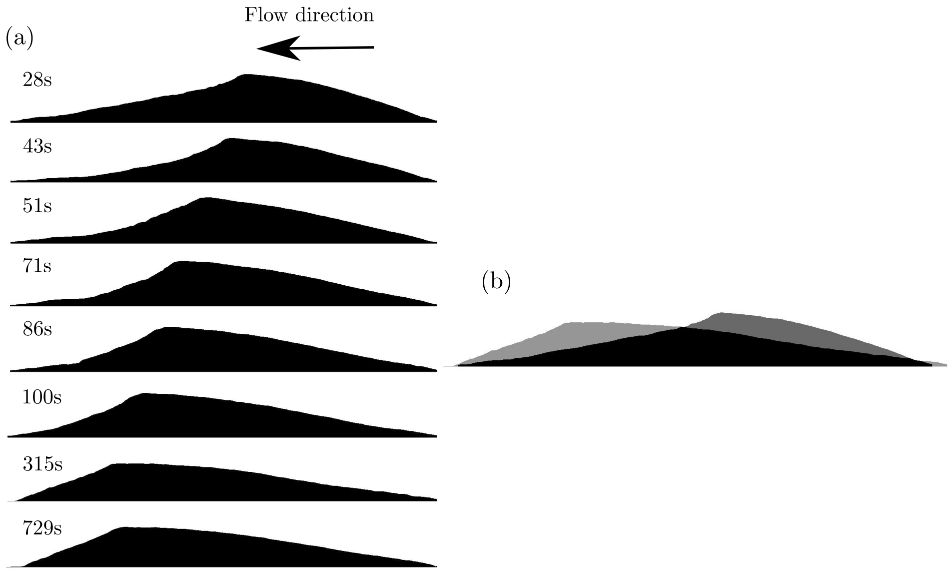

Figure 6. (a) Snapshots showing lateral-view images of an initially developed 2D dune undergoing a flow reversal for case h (Table 1). The flow is from right to left in the images, and the corresponding time instants are shown on the left (time set to 0 s at the beginnig of the reversed flow). (b) Superposition of the side view of the initial (t = 28 s, in darker gray) and developed (t = 315 s, in lighter gray) bedforms (intersection appears in black).

face, which has its slope decreased over time while the crest is displaced to the left. At the same time, a new lee face develops over the previous stoss side, with the crest and a small avalanche face migrating over it. During this process (within 28 s and 100 s in Figure 6), the new lee face has a varying angle, going from the avalanche angle (near the crest) to a very low slope (close to the new trailing edge). When the avalanche face reaches the trailing edge, the dune is properly inverted. In order to investigate further the reversal process, we measured the main morphological scales, which we present next.

Figures 7a–f show the vertical position of the maximum height (crest) of bedforms, Z/L, as a function of time, t/t_c, for cases g to l, respectively. If we neglect the small initial rise in Figures 7a–c and 7f, we observe basically the existence of three timescales: (i) a fast timescale occurring for $t/t_c < 5$, for which Z decreases over time, representing the initial flattening of the dune. During the flattening, the crest region diffuses and moves downstream, and the former avalanche face moves over the former stoss slope (between 28 s and 71s in Figure 6); (ii) a fast timescale occurring within $5 < t/t_c < 10$, for which Z increases over time. This is due to the formation of a new avalanche face over the former stoss side while the crest continues its downstream motion; and (iii) a slow timescale for $t/t_c > 10$, where Z/L remains constant or oscillates around a mean value, indicating a developed form. Therefore, the total time for achieving an inverted dune is $t/t_c \approx 10$, approximately twice that for development from an initial heap.

Following a similar procedure as for the barchan formation, we carried out CFD-DEM simulations of a barchan undergoing inversion, and analyzed the behavior of its central slice. For that, we started with the developed barchan obtained in previous simulations and reversed the flow direction. Figure 8 shows snapshots of the central slice of a barchan undergoing inversion for different instants (see the supporting information for snapshots showing top view images of the barchan dune, and a movie showing the central slice during the inversion). Although the central slice has a much smaller num-

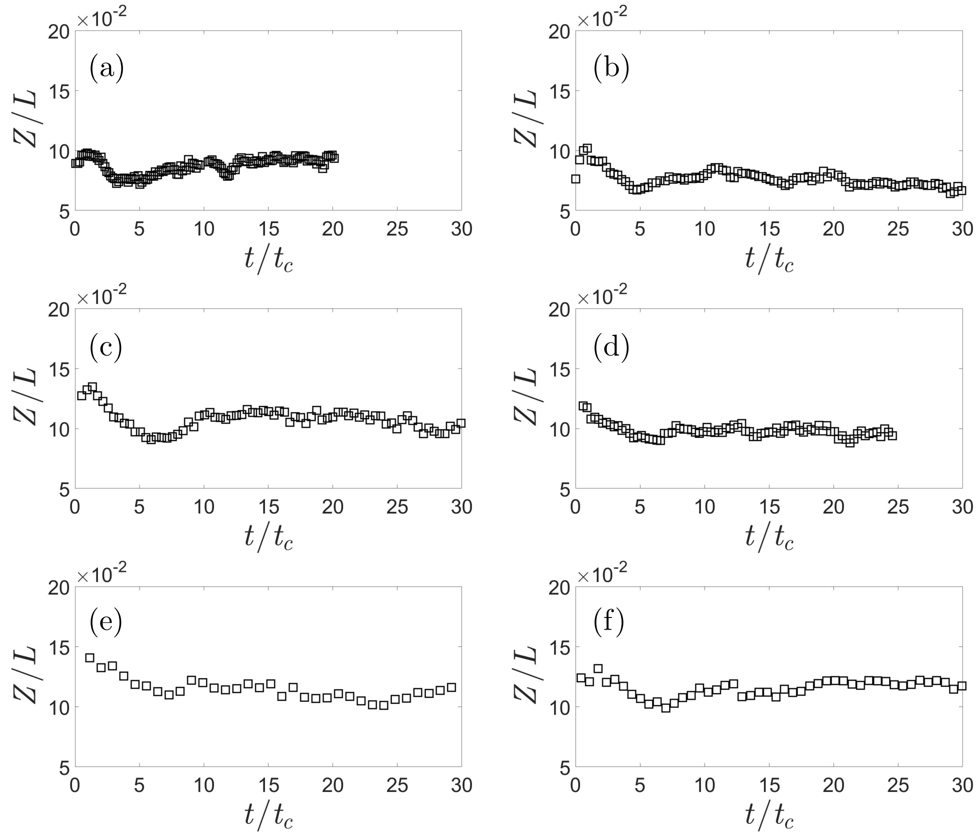

Figure 7. Vertical position of the maximum height (crest) of bedforms Z normalized by the dune length L, as a function of time t normalized by the timescale t_c. Figures (a), (c), (e) and (b), (d), (f) correspond to cases j, k, l and g, h, i (Table 1), respectively.
Figures (a) to (f) correspond to cases g to l (Table 1), respectively.

ber of grains than the 2D dune, we observe a certain similarity between them: the crest and former avalanche face move over the former stoss side, and the latter becomes the new lee side. During the inversion process, the new lee side has a varying slope that goes from a very low angle (close to the new trailing edge, former toe) to an avalanche angle (just downstream the crest). Figures showing $\theta(x)$ at different time instants for the reversing dune are available in the supporting information, for both the experiments and numerical simulations (central slice). Here, they also present a similar trend, with slightly higher mean values of $\theta(x)$ for the experiment.

In order to identify the time to attain a developed barchan, we proceeded as in Alvarez and Franklin (2017) and tracked the growth of horns. Figure 5b shows the time evolution of the horn length L_h, normalized by the characteristic length L_{drag}, for a barchan undergoing reversal. We observe that initially the existing horns shrink (L_h decreases), disappearing completely when $t/t_c \approx 1$, and from this time on the new horns begin to develop (L_h increases). When $t/t_c \approx$ 2–2.5, the new horns seem to reach a developed state (L_h reaches a plateau, oscillating around a mean value). Therefore, the barchan, as the 2D dune, takes twice the time to be completely inverted when compared with the formation from an initially conical heap.

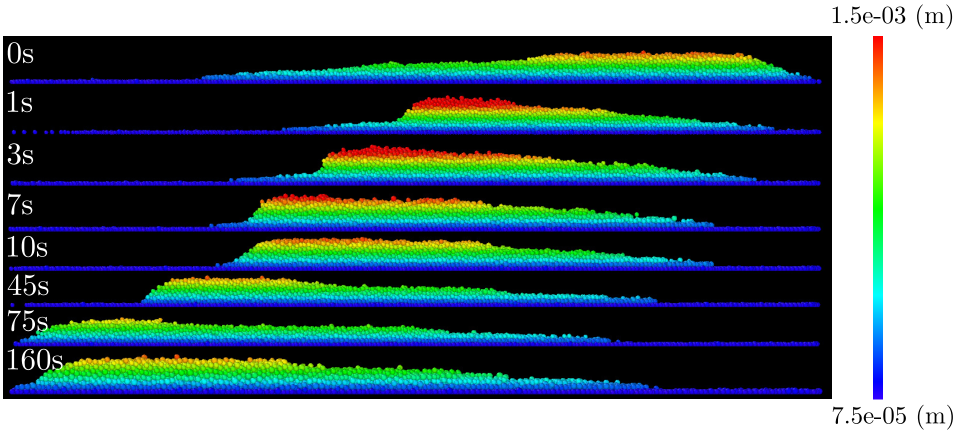

Figure 8. Snapshots showing the central slice of a barchan dune undergoing a flow reversal. The water flow is from right to left, and the color represents the height (scale in the colorbar on the right). The corresponding time instants are shown on the left.

4.3 Development vs reversal: t_c and mobility of grains

In the previous subsections, we compared 2D dunes with the central slice of 3D barchans. We found that the characteristic time for the development of 2D dunes is 5 t_c, where t_c is a timescale used for the growth of barchan dunes.We also showed that for both 2D and barchan dunes the characteristic time to completely invert the dune under a flow reversal is twice that for the dune formation. These are relevant results indicating that the central slice of a barchan dune behaves roughly as a 2D dune.

We now investigate the mobility of grains during the development and inversion of dunes. Since the numerical simulations compute the instantaneous position of each grain, we can track the motion of all grains as a function of time. Therefore, we measured the mobility of grains in the central slice during the barchan development and inversion. For example, Figure 9 shows in red the grains with instantaneous velocities greater than $0.1u_*$ (typical bedload velocity over the dune, Wenzel & Franklin, 2019). We observe that only a few grains are mobilized within the central slice at each instant: only grains close to the surface move as bedload and grain below the surface remain static until exposed.

In order to know the proportion of moving grains with respect to the total, we counted the number of grains in the central slice that moved as bedload until a developed state was reached. We obtained that approximately 23% of grains remained static during the development from the initial heap and 20% of grains remained static during the barchan reversal. We conclude that 1/5th of the grains in the central slice remain static when a dune develops from a different bedform. A description of the procedure for identifying and counting the moving grains and a table listing the instantaneous number of grains moving as bedload at each instant are available in the supporting information.

Finally, we measured the number of grains lost by the barchan dune along time. In terms of rates, we observed that during inversion the dune loses 10–15% more grains than during its formation from a conical heap, as illustrated in the supporting information by tracing the amount of particles being lost over time.

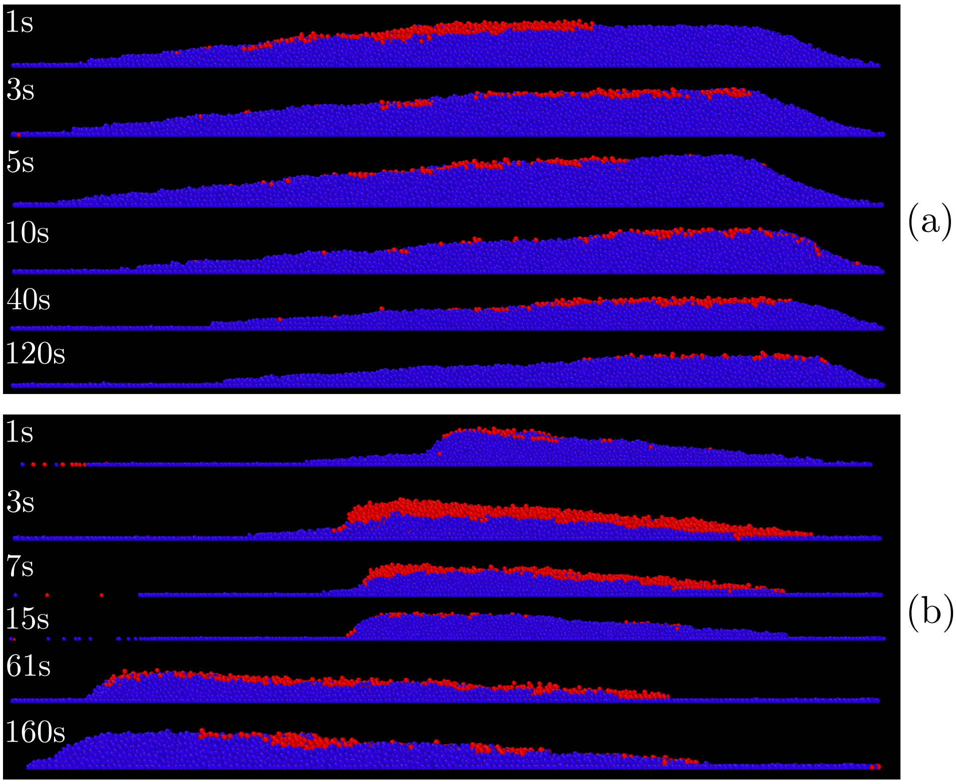

Figure 9. Snapshots showing grains being entrained as bedload (red particles) and static (blue) in the central slice of a barchan dune. (a) Development from an initial heap and (b) barchan undergoing a reversal. The corresponding time instants are shown on the left.

5 Conclusions

In this paper, we investigated the similarities between a real 2D dune and the central slice of a 3D barchan dune, and how these dunes react under flow reversals. For that, we carried out experiments in a 2D flume and CFD-DEM simulations of 3D dunes where an initial heap was deformed into a dune that, by reversing the flow, evolved afterward toward an inverted dune. We found that the characteristic time for the development of 2D dunes is 5 t_c, where t_c is a timescale used for the growth of barchan dunes. By comparing earlier work on 3D dunes, we concluded that the characteristic time-scale for 2D dunes is equivalent to that for 3D barchans. We showed that for both 2D and 3D barchan dunes the characteristic time to completely invert the dune under a flow reversal is twice that for the dune formation, and we revealed the morphodynamics of reversing dunes: the grains on the lee side climb back the dune while its internal part and toe remain static, forming a new lee face. During the inversion process, the new lee side has a varying slope that goes from a very small angle (close to the new trailing edge, former toe) to an avalanche angle (just downstream the crest). We also showed that a considerable part of grains (around 20%) remain static during the entire process, and that the barchan dune loses more grains during the reversal than during its formation from a conical pile. Our findings reveal the mechanisms for dune reversal, and provide a proof-of-concept that, in some cases, numerical similations of 3D barchans can be reduced to a central slice of a 2D dune, even in the subaqueous case.

Open Research

Data (digital images) supporting this work were generated by ourselves and are available in Mendeley Data (Assis et al., 2023) under the CC-BY-4.0 license. The numerical scripts used to process the images and the numerical setup for simulations are also available in Mendeley Data (Assis et al., 2023) under the CC-BY-4.0 license.

Acknowledgments

Willian Assis and Erick Franklin are grateful to the São Paulo Research Foundation – FAPESP (Grant Nos. 2018/14981-7, 2019/10239-7 and 2021/12910-8) and Conselho Nacional de Desenvolvimento Científico e Tecnológico – CNPq (Grant No. 405512/2022-8) for the financial support provided. N. M. Vriend is supported by a Royal Society University Research Fellowship No. URF/R1/191332. Willian Assis would like to express his gratitude to Karol Bacik and Nicolao Lima for their assistance in the experimental and numerical parts of this research, respectively.

References

Alvarez, C. A., & Franklin, E. M. (2017, Dec). Birth of a subaqueous barchan dune. *Phys. Rev. E*, *96*, 062906. Retrieved from `https://link.aps.org/doi/10.1103/PhysRevE.96.062906` doi: 10.1103/PhysRevE.96.062906

Alvarez, C. A., & Franklin, E. M. (2018, Oct). Role of transverse displacements in the formation of subaqueous barchan dunes. *Phys. Rev. Lett.*, *121*, 164503. Retrieved from `https://link.aps.org/doi/10.1103/PhysRevLett.121.164503` doi: 10.1103/PhysRevLett.121.164503

Alvarez, C. A., & Franklin, E. M. (2019, Oct). Horns of subaqueous barchan dunes: A study at the grain scale. *Phys. Rev. E*, *100*, 042904. Retrieved from `https://link.aps.org/doi/10.1103/PhysRevE.100.042904` doi: 10.1103/PhysRevE.100.042904

Alvarez, C. A., & Franklin, E. M. (2020, Jan). Shape evolution of numerically obtained subaqueous barchan dunes. *Phys. Rev. E*, *101*, 012905. Retrieved from `https://link.aps.org/doi/10.1103/PhysRevE.101.012905` doi: 10.1103/PhysRevE.101.012905

Alvarez, C. A., & Franklin, E. M. (2021). Force distribution within a barchan dune. *Phys. Fluids*, *33*(1), 013313.

Andreotti, B., Claudin, P., & Douady, S. (2002). Selection of dune shapes and velocities. part 1: Dynamics of sand, wind and barchans. *Eur. Phys. J. B*, *28*, 321-329.

Andreotti, B., Fourrière, A., Ould-Kaddour, F., Murray, B., & Claudin, P. (2009). Giant aeolian dune size determined by the average depth of the atmospheric boundary layer. *Nature*, *457*, 1120-1123.

Assis, W. R., & Franklin, E. M. (2020). A comprehensive picture for binary interactions of subaqueous barchans. *Geophys. Res. Lett.*, *47*(18), e2020GL089464.

Assis, W. R., & Franklin, E. M. (2021). Morphodynamics of barchan-barchan interactions investigated at the grain scale. *J. Geophys. Res.: Earth Surf.*, *126*(8), e2021JF006237.

Assis, W. R., Franklin, E. M., & Vriend, N. M. (2023). Dataset for "evolving dunes under flow reversals: from an initial heap toward inverted dune" [Dataset][Software]. *Mendeley Data, http://dx.doi.org/10.17632/fw3bcrxknf.1*. doi: 10.17632/fw3bcrxknf.1

Bacik, K. A., Canizares, P., Caulfield, C.-c. P., Williams, M. J., & Vriend, N. M. (2021, Oct). Dynamics of migrating sand dunes interacting with obstacles. *Phys. Rev. Fluids*, *6*, 104308. Retrieved from `https://link.aps.org/doi/10.1103/PhysRevFluids.6.104308` doi: 10.1103/PhysRevFluids.6.104308

Bacik, K. A., Caulfield, C.-c. P., & Vriend, N. M. (2021, Oct). Stability of the interaction between two sand dunes in an idealized laboratory experiment. *Phys. Rev. Lett.*, *127*, 154501. Retrieved from `https://link.aps.org/doi/10.1103/PhysRevLett.127.154501` doi: 10.1103/PhysRevLett.127.154501

Bacik, K. A., Lovett, S., Caulfield, C.-c. P., & Vriend, N. M. (2020, Feb). Wake induced long range repulsion of aqueous dunes. *Phys. Rev. Lett.*, *124*, 054501. Retrieved from `https://link.aps.org/doi/10.1103/PhysRevLett.124.054501` doi: 10.1103/PhysRevLett.124.054501

Bagnold, R. A. (1941). *The physics of blown sand and desert dunes.* London: Chapman and Hall.

Berger, R., Kloss, C., Kohlmeyer, A., & Pirker, S. (2015). Hybrid parallelization of the LIGGGHTS open-source DEM code. *Powder Technology*, *278*, 234-247.

Claudin, P., & Andreotti, B. (2006). A scaling law for aeolian dunes on Mars, Venus, Earth, and for subaqueous ripples. *Earth Plan. Sci. Lett.*, *252*, 20-44.

Courrech du Pont, S. (2015). Dune morphodynamics. *C. R. Phys.*, *16*(1), 118 - 138.

Elbelrhiti, H., Claudin, P., & Andreotti, B. (2005). Field evidence for surface-wave-induced instability of sand dunes. *Nature*, *437*(04058).

Franklin, E. M., & Charru, F. (2011). Subaqueous barchan dunes in turbulent shear flow. Part 1. Dune motion. *J. Fluid Mech.*, *675*, 199-222.

Goniva, C., Kloss, C., Deen, N. G., Kuipers, J. A. M., & Pirker, S. (2012). Influence of rolling friction on single spout fluidized bed simulation. *Particuology*, *10*(5), 582-591.

Guignier, L., Niiya, H., Nishimori, H., Lague, D., & Valance, A. (2013, May). Sand dunes as migrating strings. *Phys. Rev. E*, *87*, 052206. Retrieved from `https://link.aps.org/doi/10.1103/PhysRevE.87.052206` doi: 10.1103/PhysRevE.87.052206

Herrmann, H. J., & Sauermann, G. (2000). The shape of dunes. *Physica A (Amsterdam)*, *283*, 24-30.

Hersen, P. (2004). On the crescentic shape of barchan dunes. *Eur. Phys. J. B*, *37*(4), 507–514.

Hersen, P., Andersen, K. H., Elbelrhiti, H., Andreotti, B., Claudin, P., & Douady, S. (2004, Jan). Corridors of barchan dunes: Stability and size selection. *Phys. Rev. E*, *69*, 011304. Retrieved from `https://link.aps.org/doi/10.1103/PhysRevE.69.011304` doi: 10.1103/PhysRevE.69.011304

Hersen, P., Douady, S., & Andreotti, B. (2002, Dec). Relevant length scale of barchan dunes. *Phys. Rev. Lett.*, *89*, 264301. Retrieved from `https://link.aps.org/doi/10.1103/PhysRevLett.89.264301` doi: 10.1103/PhysRevLett.89.264301

Jarvis, P., Bacik, K., Narteau, C., & Vriend, N. (2022). Coarsening dynamics of 2d subaqueous dunes. *Journal of Geophysical Research: Earth Surface*, *127*(2), e2021JF006492.

Khosronejad, A., & Sotiropoulos, F. (2017). On the genesis and evolution of barchan dunes: morphodynamics. *J. Fluid Mech.*, *815*, 117–148.

Kidanemariam, A. G., & Uhlmann, M. (2014). Direct numerical simulation of pattern formation in subaqueous sediment. *J. Fluid Mech.*, *750*, R2.

Kloss, C., & Goniva, C. (2010). LIGGGHTS: a new open source discrete element simulation software. In *Proc. 5th int. conf. on discrete element methods.* London, UK.

Kroy, K., Fischer, S., & Obermayer, B. (2005). The shape of barchan dunes. *J. Phys. Condens. Matter*, *17*, S1229-0S1235.

Kroy, K., Sauermann, G., & Herrmann, H. J. (2002a, Sep). Minimal model for aeolian sand dunes. *Phys. Rev. E*, *66*, 031302. Retrieved from `https://link.aps.org/doi/10.1103/PhysRevE.66.031302` doi: 10.1103/PhysRevE.66.031302

Kroy, K., Sauermann, G., & Herrmann, H. J. (2002b, Jan). Minimal model for sand dunes. *Phys. Rev. Lett.*, *88*, 054301. Retrieved from `https://link.aps.org/`

doi/10.1103/PhysRevLett.88.054301 doi: 10.1103/PhysRevLett.88.054301

Lima, N. C., Assis, W. R., Alvarez, C. A., & Franklin, E. M. (2022). Grain-scale computations of barchan dunes. *Phys. Fluids*, *34*(12), 123320. Retrieved from https://doi.org/10.1063/5.0121810 doi: 10.1063/5.0121810

Pähtz, T., Kok, J. F., Parteli, E. J. R., & Herrmann, H. J. (2013). Flux saturation length of sediment transport. *Phys. Rev. Lett.*, *111*, 218002.

Parteli, E. J. R., Andrade, J. S., & Herrmann, H. J. (2011, Oct). Transverse instability of dunes. *Phys. Rev. Lett.*, *107*, 188001. Retrieved from https://link.aps.org/doi/10.1103/PhysRevLett.107.188001 doi: 10.1103/PhysRevLett.107.188001

Parteli, E. J. R., Durán, O., Bourke, M. C., Tsoar, H., Pöschel, T., & Herrmann, H. (2014). Origins of barchan dune asymmetry: Insights from numerical simulations. *Aeol. Res.*, *12*, 121-133.

Parteli, E. J. R., Durán, O., & Herrmann, H. J. (2007, Jan). Minimal size of a barchan dune. *Phys. Rev. E*, *75*, 011301. Retrieved from https://link.aps.org/doi/10.1103/PhysRevE.75.011301 doi: 10.1103/PhysRevE.75.011301

Parteli, E. J. R., & Herrmann, H. J. (2007, Oct). Dune formation on the present mars. *Phys. Rev. E*, *76*, 041307. Retrieved from https://link.aps.org/doi/10.1103/PhysRevE.76.041307 doi: 10.1103/PhysRevE.76.041307

Sauermann, C., Rognon, P., Poliakov, A., & Herrmann, H. J. (2000). The shape of the barchan dunes of Southern Morocco. *Geomorphology*, *36*, 47-62.

Sauermann, G., Kroy, K., & Herrmann, H. J. (2001, Aug). Continuum saltation model for sand dunes. *Phys. Rev. E*, *64*, 031305. Retrieved from https://link.aps.org/doi/10.1103/PhysRevE.64.031305 doi: 10.1103/PhysRevE.64.031305

Schwämmle, V., & Herrmann, H. J. (2005). A model of barchan dunes including lateral shear stress. *Eur. Phys. J. E*, *16*(1), 57-65.

Wenzel, J. L., & Franklin, E. M. (2019). Velocity fields and particle trajectories for bed load over subaqueous barchan dunes. *Granular Matter*, *21*, 321-334.

Zhang, D., Yang, X., Rozier, O., & Narteau, C. (2014). Mean sediment residence time in barchan dunes. *J. Geophys. Res.: Earth Surf.*, *119*(3), 451–463.

Evolving dunes under flow reversals: from an initial heap toward an inverted dune

W. R. Assis[1], E. M. Franklin[1], N. M. Vriend[2,3,4,5]

[1]School of Mechanical Engineering, UNICAMP - University of Campinas, Rua Mendeleyev, 200, Campinas, SP, Brazil
[2]BP Institute, University of Cambridge, Cambridge, UK
[3]Department of Applied Mathematics and Theoretical Physics, University of Cambridge, Cambridge, UK
[4]Department of Earth Sciences, University of Cambridge, Cambridge, UK
[5]Current address: Department of Mechanical Engineering, University of Colorado Boulder, Boulder, USA

Key Points:

- Experiments show that 2D dunes grow and develop over a characteristic time that matches that of fully 3D barchan dunes
- The morphodynamics of reversing dunes over time are revealed by fully reversing the flow direction and tracking the rebuilding and reshaping
- Numerical simulations on a reversing 3D barchan show that its central slice behaves as the reversing 2D dunes

Corresponding author: Willian Assis, `righiassis@gmail.com`

Abstract

Sand dunes are ubiquitous in nature, and are found in abundance on Earth and other planetary environments. One of the most common types are crescent-shaped dunes known as barchans, whose mid-line could be assumed to behave as 2D dunes. In this work, we (i) compare the morphology of the mid-line of 3D barchans with 2D dunes; and (ii) track the evolution of 3D barchan and 2D dunes under bi-modal changes in the flow direction. We performed experiments in a 2D flume on 2D dunes and Euler-Lagrange simulations of 3D bedforms. The reversal experiments start with an initial heap deforming into a steady-state dune, which is then perturbed by reversing the flow, resulting in an inverted dune. We show that during the reversal the grains on the lee side immediately climb back onto the dune while its internal part and toe remain static, forming a new lee face on the previous stoss slope of varying angle. We determine that (i) the characteristic time for the development of 2D dunes scales identically with that for 3D barchans, (ii) that the time for dune reversal is twice the time necessary to develop an initial heap to steady-state, and (iii) that a considerable part of grains remain static during the entire process. Our findings reveal the mechanisms for dune reversal, and highlight that numerical computations of 2D barchans, which are more feasible in geophysical scales, predict realistic outcomes for the relevant time-scales.

Plain Language Summary

Crescent-shaped dunes, known as barchans, are found in abundance on Earth and other planetary environments. Although their different shapes and manifestations intrigue us and produce fascinating images, the underlying physics still challenges us. Here we investigate two critical questions: (i) can we capture all relevant physical processes of 3D dunes in a 2D slice? and (ii) how does the dune morph over space and time upon flow reversal (e.g. the wind blowing from the opposite direction)? We research these questions by carrying out experiments with 2D dunes in a water flume and numerical simulations of 3D barchans, and flip-around our flow forcing to investigate flow reversal. We find that the typical development times for 2D and 3D dunes are equivalent and reveal details of the rebuilding processes of the dune upon flow reversals. Interestingly, the inversion time after flow reversal is twice that of the formation time of the initial heap, and a considerable part of grains remains static during the entire process. Our findings reveal the mechanisms for dune reversal and show that 2D simulations, which are simpler and faster, reproduce the underlying physics.

1 Introduction

Sand dunes are bedforms resulting from erosion and deposition of sand by the action of a fluid flow (Bagnold, 1941; Hersen et al., 2002), and they are frequently found on Earth, Mars and other celestial bodies (Hersen, 2004; Elbelrhiti et al., 2005; Claudin & Andreotti, 2006; Parteli & Herrmann, 2007; Courrech du Pont, 2015). Among the most common are crescent-shaped dunes, known as barchans, that appear under an one-directional flow regime and when the quantity of available sand is limited.

Given the abundance of barchans present in nature, a considerable number of field measurements, experiments, and numerical simulations were conducted over the last decades (C. Sauermann et al., 2000; Hersen et al., 2002; Andreotti et al., 2002; Hersen et al., 2004; Hersen, 2004; Kroy et al., 2005, 2002b; Parteli et al., 2007; Andreotti et al., 2009; Franklin & Charru, 2011; Pähtz et al., 2013; Kidanemariam & Uhlmann, 2014; Guignier et al., 2013; Parteli et al., 2011; Khosronejad & Sotiropoulos, 2017), but only very few of them were carried out at the grain scale (Alvarez & Franklin, 2018, 2019, 2020, 2021; Assis & Franklin, 2020, 2021). Most analytical models and numerical simulations are based on information from field measurements on aeolian dunes, so that they solve the problem at the bedform scale only by considering that the grains move mainly in the longitudinal direction (typical of aeolian saltation). For example, the first numerical simulations considered the granular system as a continuum medium, some of them modeling 3D dunes as vertical slices that behave as 2D dunes. Those models hypothesize that grains move in the longitudinal direction, while transverse diffusion transfers a small quantity of mass between adjoining slices (G. Sauermann et al., 2001; Herrmann & Sauermann, 2000; Kroy et al., 2002a, 2002b, 2005; Schwämmle & Herrmann, 2005; Parteli et al., 2014). Therefore, the continuum-sliced models are, in principle, valid for aeolian barchans, which consist of a large number of grains that are entrained mainly in longitudinal direction, with small lateral motion (due to reptation). However, this is not necessarily the case of subaqueous barchans where transverse sediment transport can become dominant.

Some recent works showed that the transverse motion of grains is important for subaqueous barchans (Alvarez & Franklin, 2018, 2019), indicating that the picture of a 3D dune as connected slices must be refined in the subaqueous case. For instance, Alvarez and Franklin (2018, 2019) measured experimentally the displacement of individual grains migrating to horns as an initial pile was deformed into a barchan dune. They found that most of those grains come from upstream regions on the periphery of the dune, within angles forming 105° and 160° and 210° and 260° in the flow direction (0° pointing downstream). Those results were later corroborated by numerical simulations at the grain scale using large eddy simulation coupled with discrete element method (LES-DEM, Alvarez & Franklin, 2020, 2021; Lima et al., 2022). In this picture, grains migrating to horns have considerable transverse displacements (of the order of the dune size), contradicting, for subaqueous barchans, the models based on connected slices. Note however that the results show that grains going to horns do not come from the dune centerline.

Based on discrete simulations using a cellular automaton model, Zhang et al. (2014) found that the residence time of grains within a barchan dune, in particular in the central slice, is relatively large, being of the order of many turnover times of the barchan. They showed that the large residence time occurs because of a cyclic process: grains on the stoss side tend to disperse toward the laterals (as also shown by the experiments of Assis & Franklin, 2021), but are returned to the central region after avalanching on the lee side due to the curvature of the barchan dune. On the whole, Zhang et al. (2014) showed that transverse mixing in the central slice is restricted by this dispersion-concentration mechanism, and proposed that the central slice contains most of the information (and memory) of the barchan morphodynamics. This result is not, in principle, in contradiction with those of Alvarez and Franklin (2018, 2019), since the latter found that grains populating the horns (and afterward leaving the barchan) do not come from the central slice.

Because the interior (e.g, the central slice) of real dunes is not accessible in experiments, Bacik et al. (2020); Bacik, Caulfield, and Vriend (2021); Bacik, Canizares, et al. (2021) carried out experiments with 2D dunes in a narrow Couette-type circular water flume. Bacik et al. (2020) investigated how 2D dunes interact with each other under a turbulent water flow, and found that the turbulent structures of the flow trigger a long range dune-dune repulsion (preventing dune-dune collisions). Later Bacik, Caulfield, and Vriend (2021), inquired into the stability of a pair of dunes and proposed a parameter space where dune-dune interactions either stabilize or destabilize the initial configuration, and Bacik, Canizares, et al. (2021) showed how the presence of obstacles change the dune morphodynamics. If these findings can be proven valid for barchan dunes, they would represent a large advance toward understanding barchan fields.

Our aim is to investigate whether subaqueous 3D barchan dunes can be represented as connected slices, in essence as the 2D dune as introduced in Bacik et al. (2020); Bacik, Caulfield, and Vriend (2021); Bacik, Canizares, et al. (2021), or whether indeed the transverse sediment transport radically changes the physical behavior and needs to be accounted for. In addition, we are investigating whether the underlying physical processes of dune reversal leading to an inverted dune can be captured as a solely 2D process mimicking the mid-line of a 3D barchan dune. We are performing experiments in the 2D flume on heaps and reversing dunes and complement these experiments with numerical simulations at the grain-scale, which allows us to analyze the central slice of 3D dunes. In our numerical simulations, we apply the same forcing procedure as in our experiments: (1) pile formation, (2) development to a steady-state dune, (3) flow reversal and (4) equilibrating to a steady-state (reversed) dune. As the grains climb back up the lee side during the flow reversal stage, the internal part and the toe of the dune remain static while a new lee face with varying angle and length is formed on the former stoss slope. In this manuscript, we will identify characteristic times and scales of this reversal process, and identify the areas where the grains are remobilized in this re-morphing process. Our findings reveal the mechanisms for dune reversal and provide a validation between experimental data and numerical simulations.

2 Experimental Setup

The experimental setup is the same as used in Jarvis et al. (2022); Bacik et al. (2020), and consists of a periodic channel, a driving device, and an imaging system. The periodic channel is a circular flume with external and internal radii of 97 cm and 88 cm, respectively, filled to a level of 45.5 cm with water and particles, with parameters specified in the next paragraph. A rotating rig with 12 equidistant paddles submerged near the water surface is mounted above the flume, providing a shearing motion to the water, while the flume is connected to a counter-rotating turntable. Our tests begin by imposing a paddle rotation in the counter-clockwise direction (view from above) and a turntable rotation in the clockwise direction (we call this flow 0°). After reaching a steady-state developed dune, we revert both the paddle and turntable directions in order to obtain a reverse flow (180°). Figures 1a and 1b show a photograph and the layout of the experimental setup, respectively.

We used round glass spheres (ρ_s = 2500 kg/m^3, approximately), sieved to a diameter between 1.0 mm $\leq d \leq$ 1.3 mm, for which we consider the mean value as being $\bar{d}$ = 1.15 mm, and varied the total mass of the initial pile between 1 and 2 kg (see the supporting information for a photograph of the used particles). The flow direction was either 0° (initial flow) or 180° (reverse flow), and the water velocity varied within 0.81 m/s $\leq U \leq$ 1.22 m/s. In here, the relative velocity between the table and paddles is $U = R(\Omega_p - \Omega_t)$, the outer radius is R = 97 cm, and Ω_p and Ω_t are the angular velocities of the paddles and table, respectively. The shear velocity u_* is computed based on Equation 8 of Jarvis et al. (2022), and was found to vary between 0.050 m/s $\leq u_* \leq$ 0.103 m/s. The Reynolds number $Re = Uw/\nu$ varied within 0.73 × 10^5 and 1.10 × 10^5, where w = 9 cm is the width of the channel and ν the kinematic viscosity of water. The paddle and water heights were fixed for all tests, being 34.5 and 45.5 cm, respectively. Table 1 summarizes the test conditions, and images from experiments are available in an open repository (Assis et al., 2023). For a given velocity U, the exact angular velocities Ω_p and Ω_t were chosen empirically to reduce secondary flows in order to produce 2D dunes as symmetrical as possible (lateral-view images from 2D dunes are available in the supporting information).

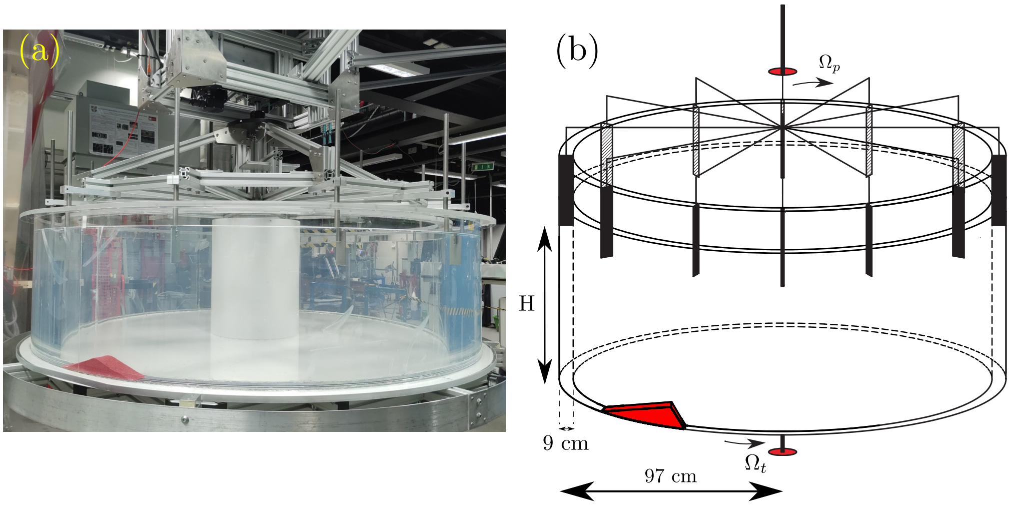

Figure 1. (a) Photograph and (b) Layout of the circular flume.

Case	Dune mass	Ω_p	Ω_t	Ω_p - Ω_t	Re	Flow direction
···	kg	rpm	rpm	rpm	···	degrees
a	2	4.60	-3.40	8	0.73×10^5	0
b	2	5.80	-4.20	10	0.91×10^5	0
c	2	7.00	-5.00	12	1.10×10^5	0
d	1	4.60	-3.40	8	0.73×10^5	0
e	1	5.65	-4.35	10	0.91×10^5	0
f	1	6.85	-5.15	12	1.10×10^5	0
g	2	-4.60	3.40	-8	0.73×10^5	180
h	2	-5.80	4.20	-10	0.91×10^5	180
i	2	-7.00	5.00	-12	1.10×10^5	180
j	1	-4.60	3.40	-8	0.73×10^5	180
k	1	-5.65	4.35	-10	0.91×10^5	180
l	1	-6.85	5.15	-12	1.10×10^5	180

Table 1. Label of tested cases, dune mass, angular velocity of paddles, angular velocity of the table, total angular velocity, channel Reynolds number Re, and flow orientation.

A camera of complementary metal-oxide-semiconductor (CMOS) type was mounted with a lateral view (i.e., in the radial direction) of the flume. We used a ISVI black and white camera, capable of acquiring images at a maximum resolution of 12MP at 181 Hz (model IC-X12S-CXP), and a Nikon lens of 60 mm focal distance and F2.8 maximum aperture (model AF Micro Nikkor). In the experiments, we set the camera to operate with a region of interest (ROI) of 64 px × 1,024 px at a frequency of 200 Hz. The field of view was 6.6 mm × 105.5 mm, corresponding to a resolution of 9.7 px/mm. A column in the central axis of the rotating experiment (see Figure 1) was illuminated with lamps of light-emitting diode (LED), enabling a good contrast between the sediment layers and walls. The acquired images were afterward processed by numerical scripts that identify and reconstruct 2D profiles providing a dune shape.

3 Numerical Setup

We carried out numerical simulations using CFD-DEM (computational fluid dynamics - discrete element method), in which we computed the formation of single barchans from initially conical piles and, after reaching a developed barchan shape, reversed the flow direction. Our simulations were performed at the grain scale by making use of LES (large eddy simulation) for CFD, which thus computed the mass (Equation 1) and momentum (Equation 2) equations for the fluid using meshes of the order of the grains' diameter,

$$\nabla \cdot \vec{u}_f = 0\,, \tag{1}$$

$$\frac{\partial \rho_f \vec{u}_f}{\partial t} + \nabla \cdot (\rho_f \vec{u}_f \vec{u}_f) = -\nabla P + \nabla \cdot \vec{\vec{\tau}} + \rho_f \vec{g} - \vec{f}_{fp}\,, \tag{2}$$

where $\vec{g}$ is the acceleration of gravity, $\vec{u}_f$ is the fluid velocity, ρ_f is the fluid density, P the fluid pressure, $\vec{\vec{\tau}}$ the deviatoric stress tensor of the fluid, and $\vec{f}_{fp}$ is the resultant of fluid forces acting on each grain by unit of fluid volume. The DEM solved the linear (Equation 3) and angular (Equation 4) momentum equations applied to each solid particle,

$$m_p \frac{d\vec{u}_p}{dt} = \vec{F}_p\,, \tag{3}$$

$$I_p \frac{d\vec{\omega}_p}{dt} = \vec{T}_c\,, \tag{4}$$

where, for each grain, m_p is the mass, $\vec{u}_p$ is the velocity, I_p is the moment of inertia, $\vec{\omega}_p$ is the angular velocity, $\vec{T}_c$ is the resultant of contact torques between solids, and $\vec{F}_p$ is the resultant force (weight, contact and fluid forces). We made use of the open-source code CFDEM (Goniva et al., 2012) (www.cfdem.com), which couples the open-source CFD code OpenFOAM with the open-source DEM code LIGGGHTS (Kloss & Goniva, 2010; Berger et al., 2015). A complete description of the fundamental and implemented equations, CFD meshes and convergence, DEM parameters, and tests can be found in Lima et al. (2022).

The CFD domain is a 3D channel of size $L_x = 0.4$ m, $L_y = \delta = 0.025$ m and $L_z = 0.1$ m, where x, y and z are the longitudinal, vertical and spanwise directions, respectively, with periodic conditions in the longitudinal and spanwise directions. The vertical dimension of the domain, $L_y = \delta$, corresponds to the channel half height (the real channel height being 2δ), and the height of smallest meshes (close to the bottom boundary) was $\Delta y = 2.9 \times 10^{-4}$ m, which corresponds to $\Delta y/d = 1.46$ (the values of d used in the simulations are shown next). The fluid is water, flowing with a cross-sectional mean velocity $U = 0.28$ m/s. The channel Reynolds number based on U, $\mathrm{Re} = U2\delta\nu^{-1}$, is 14,000, and the Reynolds number based on shear velocity u_*, $\mathrm{Re}_* = u_*\delta\nu^{-1}$, is 400, where ν is the kinematic viscosity (10^{-6} m^2/s for water). The granular material consisted of 10^5 glass spheres randomly distributed, with sizes following a Gaussian distribution within

0.15 mm $\leq d \leq 0.25$ mm. The coefficients of sliding friction μ, rolling friction μ_r and restitution e, as well as the values of Poisson ratio σ, Young's modulus E and density ρ_p used in the simulations are shown in Table 2 (extensive tests of these parameters are presented in Lima et al., 2022). We selected for the particles a solid wall boundary condition at the bottom boundary, and a free exit at the outlet. Note that no influx of grains was imposed, so that the bedform lose grains and decrease slightly in size along time. We note also that the numerical setup differs from the experimental one in terms of fluid flow, grain diameter, boundary conditions, and size of the system. While, on the one hand, to simulate barchans with a size comparable to the 2D experiments would be computationally unfeasible, on the other hand the numerical setup used has been extensively investigated and validated against experiments (Lima et al., 2022). In addition, the use of periodic conditions for the grains (to be closer to the experimental setup) would imply that grains leaving the two horns would return and reach regions close to the flanks of the barchan dune, deforming it considerably. More details about the equations, parameters and meshes used in the simulations can be found in Lima et al. (2022).

Table 2. Physical properties of DEM particles.

DEM properties	
Sliding Friction Coeff. μ	0.6
Rolling Friction Coeff. μ_r	0.00
Restitution Coef. e	0.1
Poisson Ratio σ	0.45
Young's Modulus E (MPa)	5
Density ρ_p (kg/m^3)	2500

The first step was to simulate a pure fluid (in the absence of solid particles) flowing in the periodic channel until reaching fully-developed turbulence, and store the output to be used as initial condition in the CFD-DEM simulations (which are periodic only for the fluid). This step aimed at obtaining the initial conditions for the fluid with relatively low computational cost. Then, prior to each simulation, the grains are allowed to fall freely in stationary water, forming a conical heap in the channel center. Finally, the CFD-DEM simulations begin by imposing a turbulent water flow (whose initial condition was the previously stored fully-turbulent flow), which deforms the conical pile into a barchan dune. When a developed barchan is achieved, the flow is stopped and its direction reversed. Files with the setups used in our CFD-DEM simulations are available in an open repository (Assis et al., 2023).

4 Results and Discussion

4.1 Development of a dune from an initial heap

For the experiments outlined in cases a to f (Table 1), we followed the bedform as it evolves from an initial heap into a 2D dune. For example, Figure 2 shows reconstructed snapshots of an initial pile being deformed into a 2D dune for case c. We initially observe the elongation of the upstream side and the formation of an avalanche face downstream of the crest, with the corresponding decrease of the crest height. Afterward, from a certain time on (76 s in this case), the dune keeps roughly the same shape, indicating a developed state. On the right, Figure 2 shows the superposition of the side view of the initial (t = 4 s, in darker gray) and developed (t = 76 s, in lighter gray) dunes. Because the intersected area (in black) is proportional to the number of grains that did not move (not necessarily equal, though), it indicates that a considerable part of the dune remains static, and that the dune reaches its developed form prior to a complete turnover.

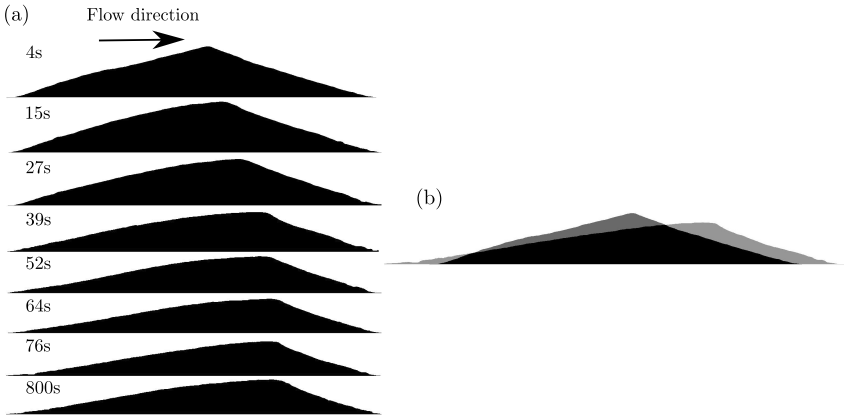

Figure 2. (a) Snapshots showing lateral-view images of an initial heap being deformed into a 2D dune for case c (Table 1). The flow is from left to right in the images, and the corresponding time instants are shown on the left. (b) Superposition of the side view of the initial ($t = 4$ s, in darker gray) and developed ($t = 76$ s, in lighter gray) bedforms (intersection appears in black).

In order to investigate further the dune development, we measured the main morphological scales (length L, height Z and slope θ) along time.

Figures 3a–f present the vertical position of the maximum height (crest) of bedforms, Z, as a function of time, t, for cases a to f, respectively. In this figure, Z is normalized by the dune length in the streamwise direction, L, and time t_c which is a timescale for the growth of subaqueous barchans proposed by Alvarez and Franklin (2017),

$$t_c = \frac{L_{eq}(\rho_p/\rho)(\rho_p/\rho - 1)gd}{(u_*^2 - u_{th}^2)^{3/2}} \ , \tag{5}$$

where u_{th} is shear velocity at the threshold for the incipient motion of grains, L_{eq} is the length of the developed dune, and $g = |\vec{g}|$. Because t_c in Equation 5 is proportional to L_{eq} divided by the dune celerity (displacement velocity of the dune crest), it scales with the dune turnover time. In Equation 5, we computed the threshold velocity in accordance with Andreotti et al. (2002).

For all cases, we observe in Figure 3 the existence of two timescales: a fast timescale occurring for $t/t_c < 5$, where Z/L decreases relatively fast, and a slow one for $t/t_c > 10$, where Z/L remains constant or oscillates around a mean value (plateau). While the fast timescale represents the flattening of the initial heap being deformed into a dune, the slow timescale indicates the presence of a developed dune. Therefore, the intersection between those two scales corresponds to the typical time for the formation of a 2D dune from an initial heap, for which we find $t/t_c \approx 5$. This value is higher, but of the same order of magnitude, of that found by Alvarez and Franklin (2017) for the development of barchan dunes based on the growth of their horns: $t/t_c \approx 2.5$. Because the mechanisms of barchan formation are different from those of 2D dunes, which do not have horns, this proximity of typical times is a strong indication of the existence of a similitude between the 2D dunes and the central slice of barchans. In order to inquire further into it, we performed three-dimensional CFD-DEM simulations of an initial pile being deformed into a barchan dune by a water flow, and analyze next the behavior of its central slice. Figure 4 shows snapshots of the central slice of a barchan dune (width equal to 2 mm, i.e., $10d$ for different instants (see the supporting information for snapshots showing top view images of the barchan dune, and a movie showing the time evolution of the

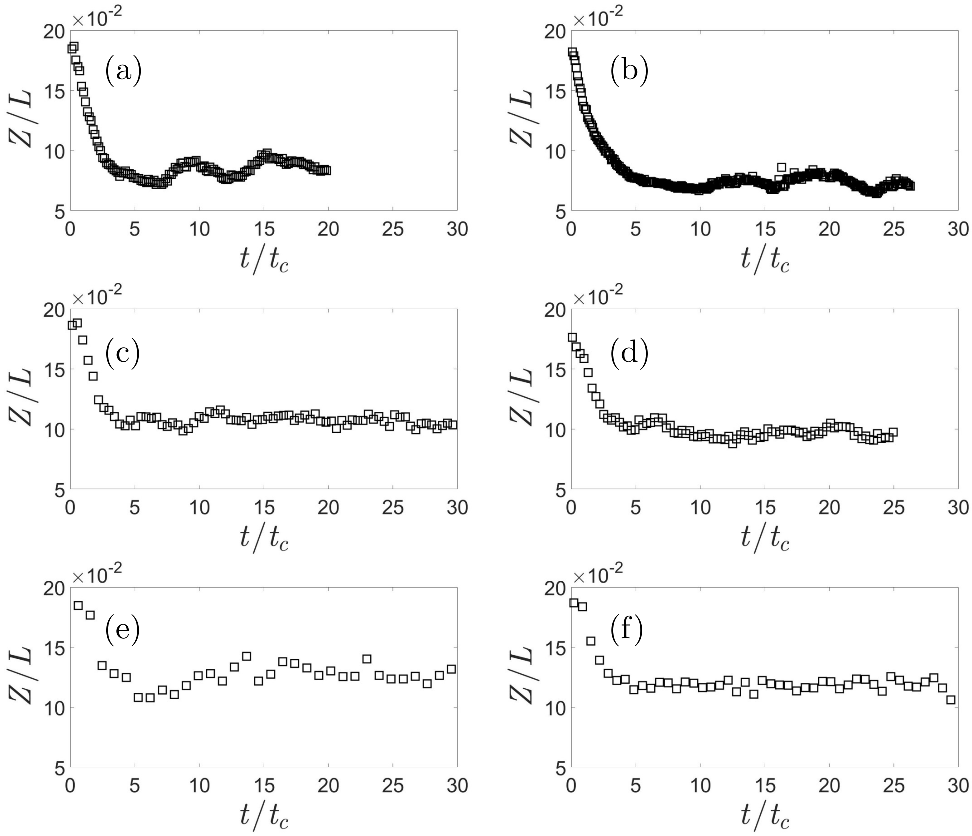

Figure 3. Vertical position of the maximum height (crest) of bedforms Z normalized by the dune length L, as a function of time t normalized by the timescale t_c. Figures (a), (c), (e) and (b), (d), (f) correspond to cases d, e, f and a, b, c (Table 1), respectively.

central slice). This width was chosen to avoid excessive fluctuations (due to the lack of grains in the spanwise direction) while analyzing the central slice only. Figures showing the longitudinal distribution of the slope, $\theta(x)$, for different time instants are available in the supporting information, for both the experiments and numerical simulations (central slice). They present a similar trend, with slightly higher mean values of $\theta(x)$ for the experiment.

In our simulations, the central slice had a much smaller number of grains than the 2D dunes, which was imposed by the computational costs of the CFD-DEM simulations (we limited the total number of grains in order to keep simulation times small). Even with this size difference, we observe that Figure 4 shows a behavior similar to that of Figure 2, with an elongation of the upstream side and formation of an avalanche face on the lee side, until a stable shape is reached (after 85 s. See figure S10 in the supporting information for the superposition of the central slice of the numerical dune). Figure 5a shows the time evolution of the horn length L_h, normalized by the characteristic length L_{drag}, as the conical pile is deformed into a barchan dune. In Figures 5a and 5b, L_h is computed as the average of the two horns, and $L_{drag} = (\rho_p/\rho_f)\, d$ is an inertial length, proportional to the flux saturation length (Hersen et al., 2002). We observe an increase in L_h along time, until a plateau is reached at $t/t_c \approx$ 1–1.5, with L_h oscillating around a mean value. The origin of oscillations are probably the small number of particles and

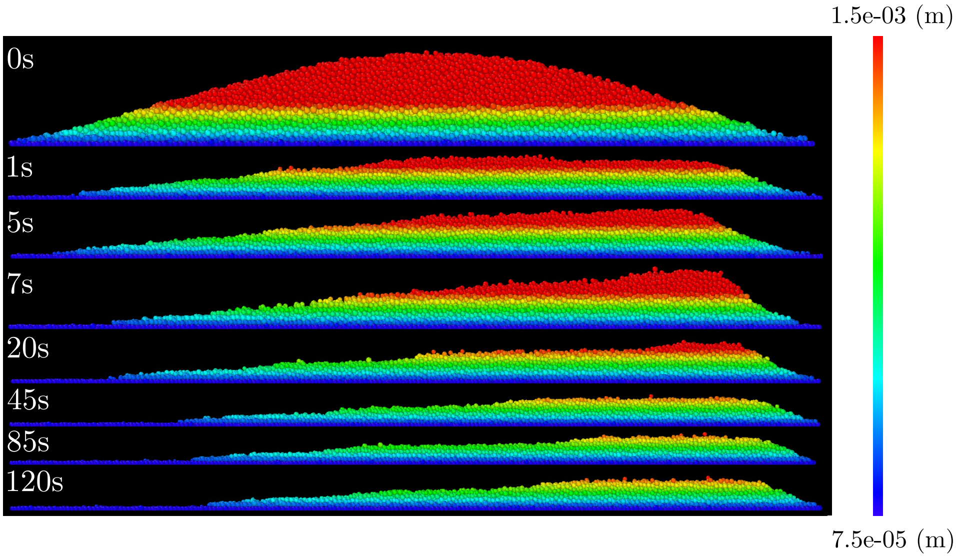

Figure 4. Snapshots showing the central slice of a bedform being deformed into a barchan dune. The water flow is from left to right and the color represents the height (scale in the colorbar on the right). The corresponding time instants are shown on the left.

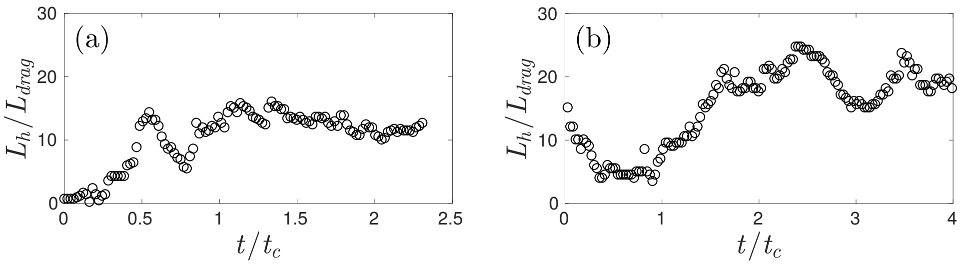

Figure 5. Time evolution of the horn length L_{horn} normalized by the characteristic length L_{drag} for (a) a barchan developed from a conical pile, and (b) for a barchan undergoing flow reversal. Results from numerical simulations, and the time is normalized by t_c.

the intermittent motion of grains. For this very small barchan, the time to reach the plateau is of the same order as that obtained experimentally by Alvarez and Franklin (2017).

In summary, by comparing the formation of 2D dunes with that of barchans from an initial heap (triangular in two and conical in three dimensions), we observe a certain similarity between them, the central slice of the barchan dune behaving roughly as a 2D dune.

4.2 Flow reversal

We inquire now into the process of inverting a dune by reversing the water flow. To create this condition, we performed experiments and numerical simulations in which we reversed the water flow after assuring that the dune was in a steady-state developed state. For the experiments with 2D dunes, this corresponds to cases g to l of Table 1. Figure 6 shows reconstructed snapshots of an initially developed 2D dune undergoing a flow reversal (case h). We notice that initially the motion occurs over the previous avalanche

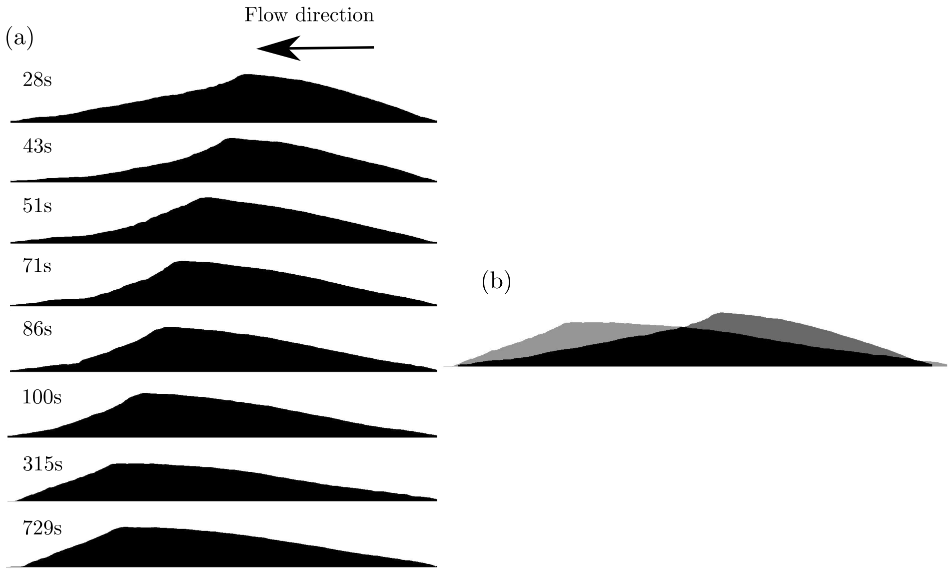

Figure 6. (a) Snapshots showing lateral-view images of an initially developed 2D dune undergoing a flow reversal for case h (Table 1). The flow is from right to left in the images, and the corresponding time instants are shown on the left (time set to 0 s at the beginnig of the reversed flow). (b) Superposition of the side view of the initial (t = 28 s, in darker gray) and developed (t = 315 s, in lighter gray) bedforms (intersection appears in black).

face, which has its slope decreased over time while the crest is displaced to the left. At the same time, a new lee face develops over the previous stoss side, with the crest and a small avalanche face migrating over it. During this process (within 28 s and 100 s in Figure 6), the new lee face has a varying angle, going from the avalanche angle (near the crest) to a very low slope (close to the new trailing edge). When the avalanche face reaches the trailing edge, the dune is properly inverted. In order to investigate further the reversal process, we measured the main morphological scales, which we present next.

Figures 7a–f show the vertical position of the maximum height (crest) of bedforms, Z/L, as a function of time, t/t_c, for cases g to l, respectively. If we neglect the small initial rise in Figures 7a–c and 7f, we observe basically the existence of three timescales: (i) a fast timescale occurring for $t/t_c < 5$, for which Z decreases over time, representing the initial flattening of the dune. During the flattening, the crest region diffuses and moves downstream, and the former avalanche face moves over the former stoss slope (between 28 s and 71s in Figure 6); (ii) a fast timescale occurring within $5 < t/t_c < 10$, for which Z increases over time. This is due to the formation of a new avalanche face over the former stoss side while the crest continues its downstream motion; and (iii) a slow timescale for $t/t_c > 10$, where Z/L remains constant or oscillates around a mean value, indicating a developed form. Therefore, the total time for achieving an inverted dune is $t/t_c \approx 10$, approximately twice that for development from an initial heap.

Following a similar procedure as for the barchan formation, we carried out CFD-DEM simulations of a barchan undergoing inversion, and analyzed the behavior of its central slice. For that, we started with the developed barchan obtained in previous simulations and reversed the flow direction. Figure 8 shows snapshots of the central slice of a barchan undergoing inversion for different instants (see the supporting information for snapshots showing top view images of the barchan dune, and a movie showing the central slice during the inversion). Although the central slice has a much smaller num-

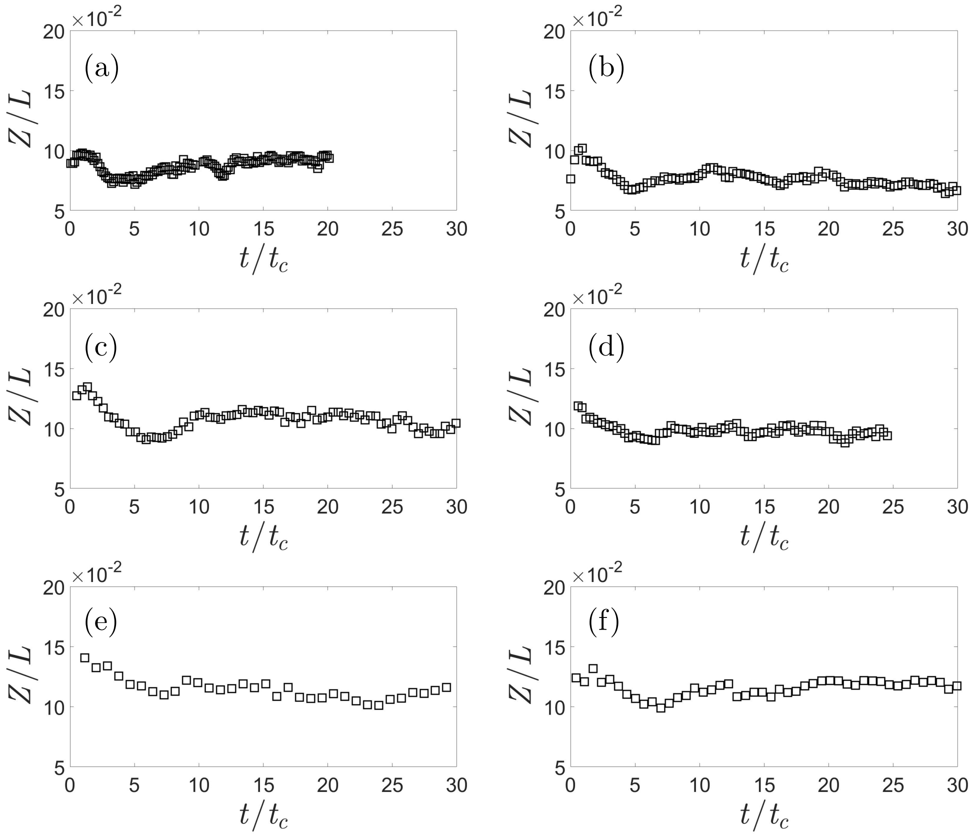

Figure 7. Vertical position of the maximum height (crest) of bedforms Z normalized by the dune length L, as a function of time t normalized by the timescale t_c. Figures (a), (c), (e) and (b), (d), (f) correspond to cases j, k, l and g, h, i (Table 1), respectively.
Figures (a) to (f) correspond to cases g to l (Table 1), respectively.

ber of grains than the 2D dune, we observe a certain similarity between them: the crest and former avalanche face move over the former stoss side, and the latter becomes the new lee side. During the inversion process, the new lee side has a varying slope that goes from a very low angle (close to the new trailing edge, former toe) to an avalanche angle (just downstream the crest). Figures showing $\theta(x)$ at different time instants for the reversing dune are available in the supporting information, for both the experiments and numerical simulations (central slice). Here, they also present a similar trend, with slightly higher mean values of $\theta(x)$ for the experiment.

In order to identify the time to attain a developed barchan, we proceeded as in Alvarez and Franklin (2017) and tracked the growth of horns. Figure 5b shows the time evolution of the horn length L_h, normalized by the characteristic length L_{drag}, for a barchan undergoing reversal. We observe that initially the existing horns shrink (L_h decreases), disappearing completely when $t/t_c \approx 1$, and from this time on the new horns begin to develop (L_h increases). When $t/t_c \approx$ 2–2.5, the new horns seem to reach a developed state (L_h reaches a plateau, oscillating around a mean value). Therefore, the barchan, as the 2D dune, takes twice the time to be completely inverted when compared with the formation from an initially conical heap.

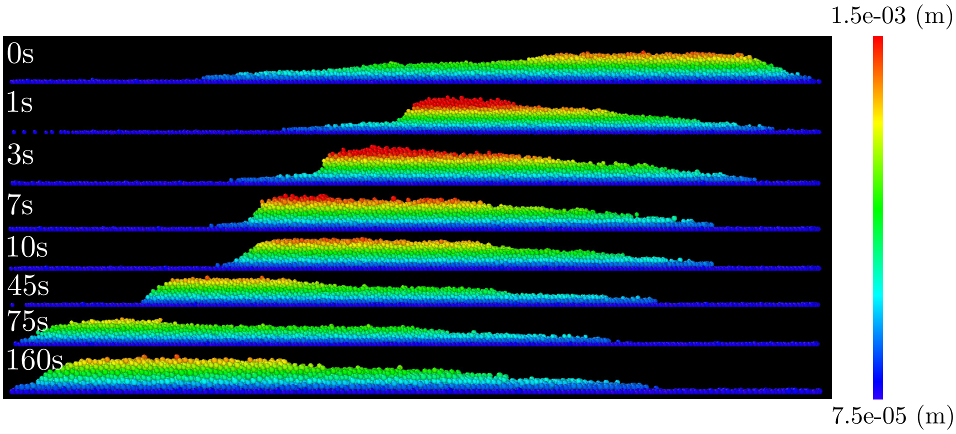

Figure 8. Snapshots showing the central slice of a barchan dune undergoing a flow reversal. The water flow is from right to left, and the color represents the height (scale in the colorbar on the right). The corresponding time instants are shown on the left.

4.3 Development vs reversal: t_c and mobility of grains

In the previous subsections, we compared 2D dunes with the central slice of 3D barchans. We found that the characteristic time for the development of 2D dunes is 5 t_c, where t_c is a timescale used for the growth of barchan dunes.We also showed that for both 2D and barchan dunes the characteristic time to completely invert the dune under a flow reversal is twice that for the dune formation. These are relevant results indicating that the central slice of a barchan dune behaves roughly as a 2D dune.

We now investigate the mobility of grains during the development and inversion of dunes. Since the numerical simulations compute the instantaneous position of each grain, we can track the motion of all grains as a function of time. Therefore, we measured the mobility of grains in the central slice during the barchan development and inversion. For example, Figure 9 shows in red the grains with instantaneous velocities greater than $0.1u_*$ (typical bedload velocity over the dune, Wenzel & Franklin, 2019). We observe that only a few grains are mobilized within the central slice at each instant: only grains close to the surface move as bedload and grain below the surface remain static until exposed.

In order to know the proportion of moving grains with respect to the total, we counted the number of grains in the central slice that moved as bedload until a developed state was reached. We obtained that approximately 23% of grains remained static during the development from the initial heap and 20% of grains remained static during the barchan reversal. We conclude that 1/5th of the grains in the central slice remain static when a dune develops from a different bedform. A description of the procedure for identifying and counting the moving grains and a table listing the instantaneous number of grains moving as bedload at each instant are available in the supporting information.

Finally, we measured the number of grains lost by the barchan dune along time. In terms of rates, we observed that during inversion the dune loses 10–15% more grains than during its formation from a conical heap, as illustrated in the supporting information by tracing the amount of particles being lost over time.

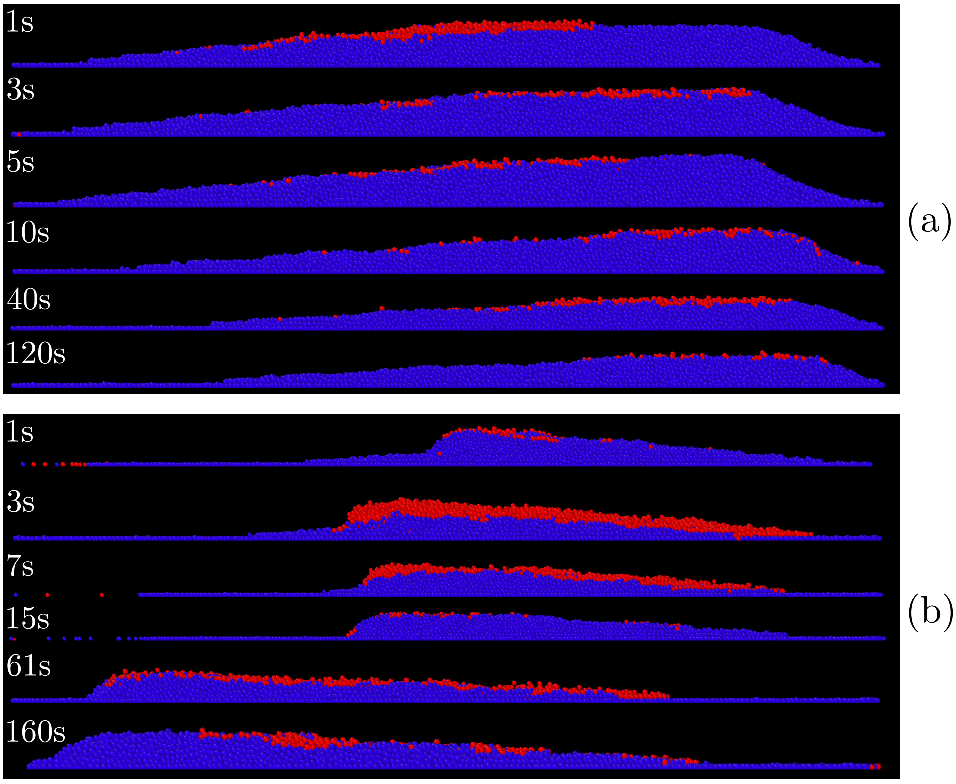

Figure 9. Snapshots showing grains being entrained as bedload (red particles) and static (blue) in the central slice of a barchan dune. (a) Development from an initial heap and (b) barchan undergoing a reversal. The corresponding time instants are shown on the left.

5 Conclusions

In this paper, we investigated the similarities between a real 2D dune and the central slice of a 3D barchan dune, and how these dunes react under flow reversals. For that, we carried out experiments in a 2D flume and CFD-DEM simulations of 3D dunes where an initial heap was deformed into a dune that, by reversing the flow, evolved afterward toward an inverted dune. We found that the characteristic time for the development of 2D dunes is 5 t_c, where t_c is a timescale used for the growth of barchan dunes. By comparing earlier work on 3D dunes, we concluded that the characteristic time-scale for 2D dunes is equivalent to that for 3D barchans. We showed that for both 2D and 3D barchan dunes the characteristic time to completely invert the dune under a flow reversal is twice that for the dune formation, and we revealed the morphodynamics of reversing dunes: the grains on the lee side climb back the dune while its internal part and toe remain static, forming a new lee face. During the inversion process, the new lee side has a varying slope that goes from a very small angle (close to the new trailing edge, former toe) to an avalanche angle (just downstream the crest). We also showed that a considerable part of grains (around 20%) remain static during the entire process, and that the barchan dune loses more grains during the reversal than during its formation from a conical pile. Our findings reveal the mechanisms for dune reversal, and provide a proof-of-concept that, in some cases, numerical similations of 3D barchans can be reduced to a central slice of a 2D dune, even in the subaqueous case.

Open Research

Data (digital images) supporting this work were generated by ourselves and are available in Mendeley Data (Assis et al., 2023) under the CC-BY-4.0 license. The numerical scripts used to process the images and the numerical setup for simulations are also available in Mendeley Data (Assis et al., 2023) under the CC-BY-4.0 license.

Acknowledgments

Willian Assis and Erick Franklin are grateful to the São Paulo Research Foundation – FAPESP (Grant Nos. 2018/14981-7, 2019/10239-7 and 2021/12910-8) and Conselho Nacional de Desenvolvimento Científico e Tecnológico – CNPq (Grant No. 405512/2022-8) for the financial support provided. N. M. Vriend is supported by a Royal Society University Research Fellowship No. URF/R1/191332. Willian Assis would like to express his gratitude to Karol Bacik and Nicolao Lima for their assistance in the experimental and numerical parts of this research, respectively.

References

Alvarez, C. A., & Franklin, E. M. (2017, Dec). Birth of a subaqueous barchan dune. *Phys. Rev. E*, *96*, 062906. Retrieved from `https://link.aps.org/doi/10.1103/PhysRevE.96.062906` doi: 10.1103/PhysRevE.96.062906

Alvarez, C. A., & Franklin, E. M. (2018, Oct). Role of transverse displacements in the formation of subaqueous barchan dunes. *Phys. Rev. Lett.*, *121*, 164503. Retrieved from `https://link.aps.org/doi/10.1103/PhysRevLett.121.164503` doi: 10.1103/PhysRevLett.121.164503

Alvarez, C. A., & Franklin, E. M. (2019, Oct). Horns of subaqueous barchan dunes: A study at the grain scale. *Phys. Rev. E*, *100*, 042904. Retrieved from `https://link.aps.org/doi/10.1103/PhysRevE.100.042904` doi: 10.1103/PhysRevE.100.042904

Alvarez, C. A., & Franklin, E. M. (2020, Jan). Shape evolution of numerically obtained subaqueous barchan dunes. *Phys. Rev. E*, *101*, 012905. Retrieved from `https://link.aps.org/doi/10.1103/PhysRevE.101.012905` doi: 10.1103/PhysRevE.101.012905

Alvarez, C. A., & Franklin, E. M. (2021). Force distribution within a barchan dune. *Phys. Fluids*, *33*(1), 013313.

Andreotti, B., Claudin, P., & Douady, S. (2002). Selection of dune shapes and velocities. part 1: Dynamics of sand, wind and barchans. *Eur. Phys. J. B*, *28*, 321-329.

Andreotti, B., Fourrière, A., Ould-Kaddour, F., Murray, B., & Claudin, P. (2009). Giant aeolian dune size determined by the average depth of the atmospheric boundary layer. *Nature*, *457*, 1120-1123.

Assis, W. R., & Franklin, E. M. (2020). A comprehensive picture for binary interactions of subaqueous barchans. *Geophys. Res. Lett.*, *47*(18), e2020GL089464.

Assis, W. R., & Franklin, E. M. (2021). Morphodynamics of barchan-barchan interactions investigated at the grain scale. *J. Geophys. Res.: Earth Surf.*, *126*(8), e2021JF006237.

Assis, W. R., Franklin, E. M., & Vriend, N. M. (2023). Dataset for "evolving dunes under flow reversals: from an initial heap toward inverted dune" [Dataset][Software]. *Mendeley Data, http://dx.doi.org/10.17632/fw3bcrxknf.1*. doi: 10.17632/fw3bcrxknf.1

Bacik, K. A., Canizares, P., Caulfield, C.-c. P., Williams, M. J., & Vriend, N. M. (2021, Oct). Dynamics of migrating sand dunes interacting with obstacles. *Phys. Rev. Fluids*, *6*, 104308. Retrieved from `https://link.aps.org/doi/10.1103/PhysRevFluids.6.104308` doi: 10.1103/PhysRevFluids.6.104308

Bacik, K. A., Caulfield, C.-c. P., & Vriend, N. M. (2021, Oct). Stability of the interaction between two sand dunes in an idealized laboratory experiment. *Phys. Rev. Lett.*, *127*, 154501. Retrieved from `https://link.aps.org/doi/10.1103/PhysRevLett.127.154501` doi: 10.1103/PhysRevLett.127.154501

Bacik, K. A., Lovett, S., Caulfield, C.-c. P., & Vriend, N. M. (2020, Feb). Wake induced long range repulsion of aqueous dunes. *Phys. Rev. Lett.*, *124*, 054501. Retrieved from `https://link.aps.org/doi/10.1103/PhysRevLett.124.054501` doi: 10.1103/PhysRevLett.124.054501

Bagnold, R. A. (1941). *The physics of blown sand and desert dunes.* London: Chapman and Hall.

Berger, R., Kloss, C., Kohlmeyer, A., & Pirker, S. (2015). Hybrid parallelization of the LIGGGHTS open-source DEM code. *Powder Technology*, *278*, 234-247.

Claudin, P., & Andreotti, B. (2006). A scaling law for aeolian dunes on Mars, Venus, Earth, and for subaqueous ripples. *Earth Plan. Sci. Lett.*, *252*, 20-44.

Courrech du Pont, S. (2015). Dune morphodynamics. *C. R. Phys.*, *16*(1), 118 - 138.

Elbelrhiti, H., Claudin, P., & Andreotti, B. (2005). Field evidence for surface-wave-induced instability of sand dunes. *Nature*, *437*(04058).

Franklin, E. M., & Charru, F. (2011). Subaqueous barchan dunes in turbulent shear flow. Part 1. Dune motion. *J. Fluid Mech.*, *675*, 199-222.

Goniva, C., Kloss, C., Deen, N. G., Kuipers, J. A. M., & Pirker, S. (2012). Influence of rolling friction on single spout fluidized bed simulation. *Particuology*, *10*(5), 582-591.

Guignier, L., Niiya, H., Nishimori, H., Lague, D., & Valance, A. (2013, May). Sand dunes as migrating strings. *Phys. Rev. E*, *87*, 052206. Retrieved from `https://link.aps.org/doi/10.1103/PhysRevE.87.052206` doi: 10.1103/PhysRevE.87.052206

Herrmann, H. J., & Sauermann, G. (2000). The shape of dunes. *Physica A (Amsterdam)*, *283*, 24-30.

Hersen, P. (2004). On the crescentic shape of barchan dunes. *Eur. Phys. J. B*, *37*(4), 507–514.

Hersen, P., Andersen, K. H., Elbelrhiti, H., Andreotti, B., Claudin, P., & Douady, S. (2004, Jan). Corridors of barchan dunes: Stability and size selection. *Phys. Rev. E*, *69*, 011304. Retrieved from `https://link.aps.org/doi/10.1103/PhysRevE.69.011304` doi: 10.1103/PhysRevE.69.011304

Hersen, P., Douady, S., & Andreotti, B. (2002, Dec). Relevant length scale of barchan dunes. *Phys. Rev. Lett.*, *89*, 264301. Retrieved from `https://link.aps.org/doi/10.1103/PhysRevLett.89.264301` doi: 10.1103/PhysRevLett.89.264301

Jarvis, P., Bacik, K., Narteau, C., & Vriend, N. (2022). Coarsening dynamics of 2d subaqueous dunes. *Journal of Geophysical Research: Earth Surface*, *127*(2), e2021JF006492.

Khosronejad, A., & Sotiropoulos, F. (2017). On the genesis and evolution of barchan dunes: morphodynamics. *J. Fluid Mech.*, *815*, 117–148.

Kidanemariam, A. G., & Uhlmann, M. (2014). Direct numerical simulation of pattern formation in subaqueous sediment. *J. Fluid Mech.*, *750*, R2.

Kloss, C., & Goniva, C. (2010). LIGGGHTS: a new open source discrete element simulation software. In *Proc. 5th int. conf. on discrete element methods.* London, UK.

Kroy, K., Fischer, S., & Obermayer, B. (2005). The shape of barchan dunes. *J. Phys. Condens. Matter*, *17*, S1229-0S1235.

Kroy, K., Sauermann, G., & Herrmann, H. J. (2002a, Sep). Minimal model for aeolian sand dunes. *Phys. Rev. E*, *66*, 031302. Retrieved from `https://link.aps.org/doi/10.1103/PhysRevE.66.031302` doi: 10.1103/PhysRevE.66.031302

Kroy, K., Sauermann, G., & Herrmann, H. J. (2002b, Jan). Minimal model for sand dunes. *Phys. Rev. Lett.*, *88*, 054301. Retrieved from `https://link.aps.org/`

doi/10.1103/PhysRevLett.88.054301 doi: 10.1103/PhysRevLett.88.054301

Lima, N. C., Assis, W. R., Alvarez, C. A., & Franklin, E. M. (2022). Grain-scale computations of barchan dunes. *Phys. Fluids*, *34*(12), 123320. Retrieved from https://doi.org/10.1063/5.0121810 doi: 10.1063/5.0121810

Pähtz, T., Kok, J. F., Parteli, E. J. R., & Herrmann, H. J. (2013). Flux saturation length of sediment transport. *Phys. Rev. Lett.*, *111*, 218002.

Parteli, E. J. R., Andrade, J. S., & Herrmann, H. J. (2011, Oct). Transverse instability of dunes. *Phys. Rev. Lett.*, *107*, 188001. Retrieved from https://link.aps.org/doi/10.1103/PhysRevLett.107.188001 doi: 10.1103/PhysRevLett.107.188001

Parteli, E. J. R., Durán, O., Bourke, M. C., Tsoar, H., Pöschel, T., & Herrmann, H. (2014). Origins of barchan dune asymmetry: Insights from numerical simulations. *Aeol. Res.*, *12*, 121-133.

Parteli, E. J. R., Durán, O., & Herrmann, H. J. (2007, Jan). Minimal size of a barchan dune. *Phys. Rev. E*, *75*, 011301. Retrieved from https://link.aps.org/doi/10.1103/PhysRevE.75.011301 doi: 10.1103/PhysRevE.75.011301

Parteli, E. J. R., & Herrmann, H. J. (2007, Oct). Dune formation on the present mars. *Phys. Rev. E*, *76*, 041307. Retrieved from https://link.aps.org/doi/10.1103/PhysRevE.76.041307 doi: 10.1103/PhysRevE.76.041307

Sauermann, C., Rognon, P., Poliakov, A., & Herrmann, H. J. (2000). The shape of the barchan dunes of Southern Morocco. *Geomorphology*, *36*, 47-62.

Sauermann, G., Kroy, K., & Herrmann, H. J. (2001, Aug). Continuum saltation model for sand dunes. *Phys. Rev. E*, *64*, 031305. Retrieved from https://link.aps.org/doi/10.1103/PhysRevE.64.031305 doi: 10.1103/PhysRevE.64.031305

Schwämmle, V., & Herrmann, H. J. (2005). A model of barchan dunes including lateral shear stress. *Eur. Phys. J. E*, *16*(1), 57-65.

Wenzel, J. L., & Franklin, E. M. (2019). Velocity fields and particle trajectories for bed load over subaqueous barchan dunes. *Granular Matter*, *21*, 321-334.

Zhang, D., Yang, X., Rozier, O., & Narteau, C. (2014). Mean sediment residence time in barchan dunes. *J. Geophys. Res.: Earth Surf.*, *119*(3), 451–463.

Supporting Information for "Evolving dunes under flow reversals: from an initial heap toward an inverted dune"

W. R. Assis[1], E. M. Franklin[1], N. M. Vriend[2,3,4,5]

[1]School of Mechanical Engineering, UNICAMP - University of Campinas, Rua Mendeleyev, 200, Campinas, SP, Brazil

[2]Department of Applied Mathematics and Theoretical Physics, University of Cambridge, Cambridge, UK

[3]BP Institute, University of Cambridge, Cambridge, UK

[4]Department of Earth Sciences, University of Cambridge, Cambridge, UK

[5]Department of Mechanical Engineering, University of Colorado Boulder, Boulder, USA

Contents of this file

1. Figures S1 to S10

Additional Supporting Information (Files uploaded separately)

1. Captions for Movies S1 to S4

Introduction

This supporting information presents a brief description of some computations (identification of moving grains and number of grains entrained further downstream), a microscopy image of the used grains, snapshots of numerical barchans, additional graphics and tables, and movies showing the motion of grains within the central slice of 3D bedforms. We note that tables, individual images and movies used in the manuscript are available on Mendeley Data, http://dx.doi.org/10.17632/fw3bcrxknf.1.

Identification of moving grains in the central slice

We carried out CFD-DEM simulations, which compute the instantaneous position of each grain. Once the simulations finished, we selected the grains within a 2-mm-thick central slice and applied a threshold above which we considered that they were moving as bedload. For that, we used the typical bedload velocity $0.1u_*$ (Wenzel and Franklin, Granular Matter, 2019). As a result, we identified the grains entrained as bedload and those static in the central slice, at each time instant. Finally, in order to compute the total number of grains that moved during the simulations, we tracked all the moving grains of the central slice along the simulation.

For the tracking of grains we did not consider the first second of simulations to avoid the relatively large initial transient. This transient was caused by imposing a fully-developed flow at $t = 0$ s, which does not occur in experiments (where the flow is accelerated gradually). The detailed description of the initial conditions in the numerical simulations, and their implications, can be found in Lima et al., Physics of Fluids, 2022.

Number of grains leaving the barchan dune

The number of grains leaving the barchan dune was computed by counting the grains that left a region around the dune and were entrained further downstream.

Captions

Movie S1. top_formation_4x.mp4 Animation from the numerical simulation showing a conical pile being deformed into a barchan dune. The animation shows top-view images of the solid spheres and is sped up 4 times.

Movie S2. top_reverse_4x.mp4 Animation from the numerical simulation showing a barchan dune being inverted under a reverse flow. The animation shows top-view images of the solid spheres and is sped up 4 times.

Movie S3. slice_formation_4x.mp4 Animation from the numerical simulation showing a conical pile being deformed into a barchan dune. The animation shows a lateral view of the the 2-mm-thick central slice and is sped up 4 times.

Movie S4. slice_reverse_4x.mp4 Animation from the numerical simulation showing a barchan dune being inverted under a reverse flow. The animation shows a lateral view of the the 2-mm-thick central slice and is sped up 4 times.

Figures

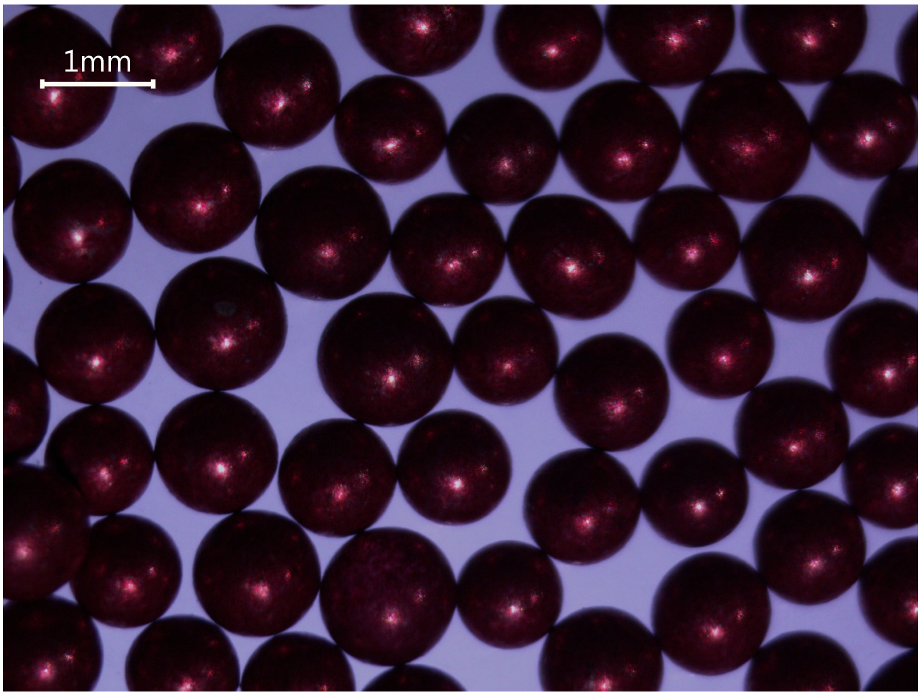

Figure S1. Microscopy image of the glass spheres used in the experiments (1.00 mm $\leq d \leq$ 1.3 mm).

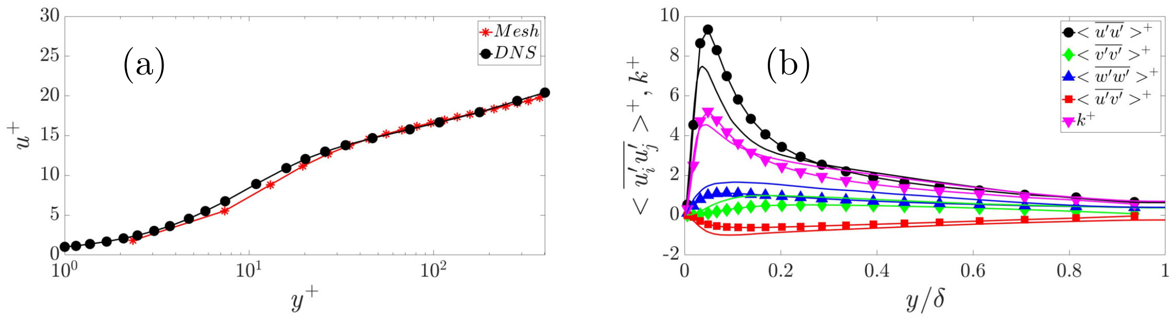

Figure S2. Mesh validation of the CFD part. (a) Mean velocity u^+ as a function of the vertical coordinate y^+; (b) turbulent kinetic energy k^+ and components of the shear stress $< \overline{u_i'u_j'} >$ as a function of y/δ. All quantities are dimensionless, the superscript + meaning normalization by the inner scales and δ corresponding to the channel half-height. DNS (direct numerical simulation) results in figure (a) are from Moser et al., Phys. Fluids 11, 943–945 (1999).

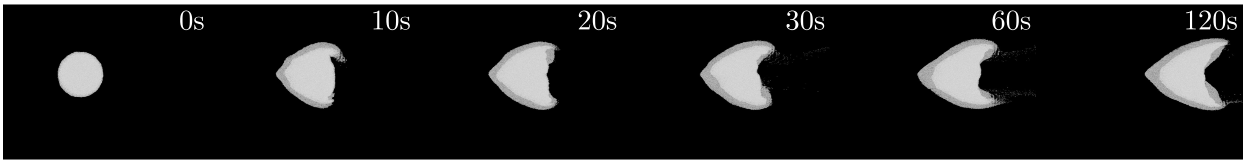

Figure S3. Snapshots from numerical simulations, showing top view images of a developing barchan from a conical pile. The flow comes from left to right in the images.

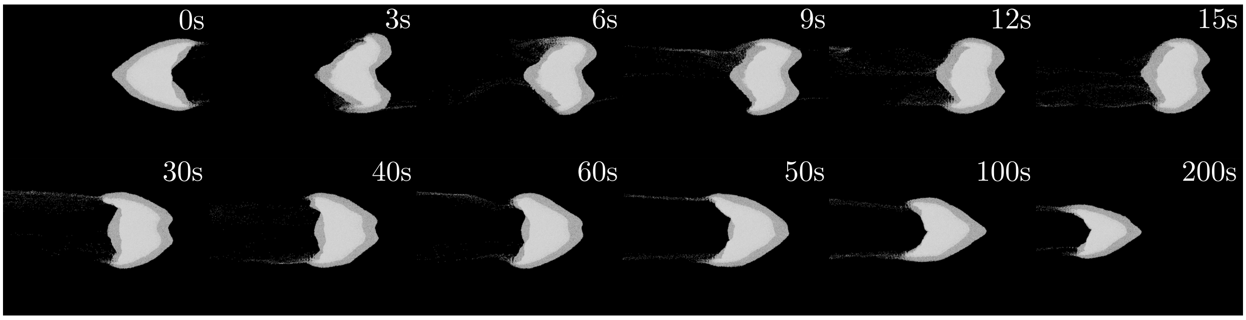

Figure S4. Snapshots from numerical simulations, showing top view images of a numerical barchan undergoing a flow reversal. The flow is from right to left.

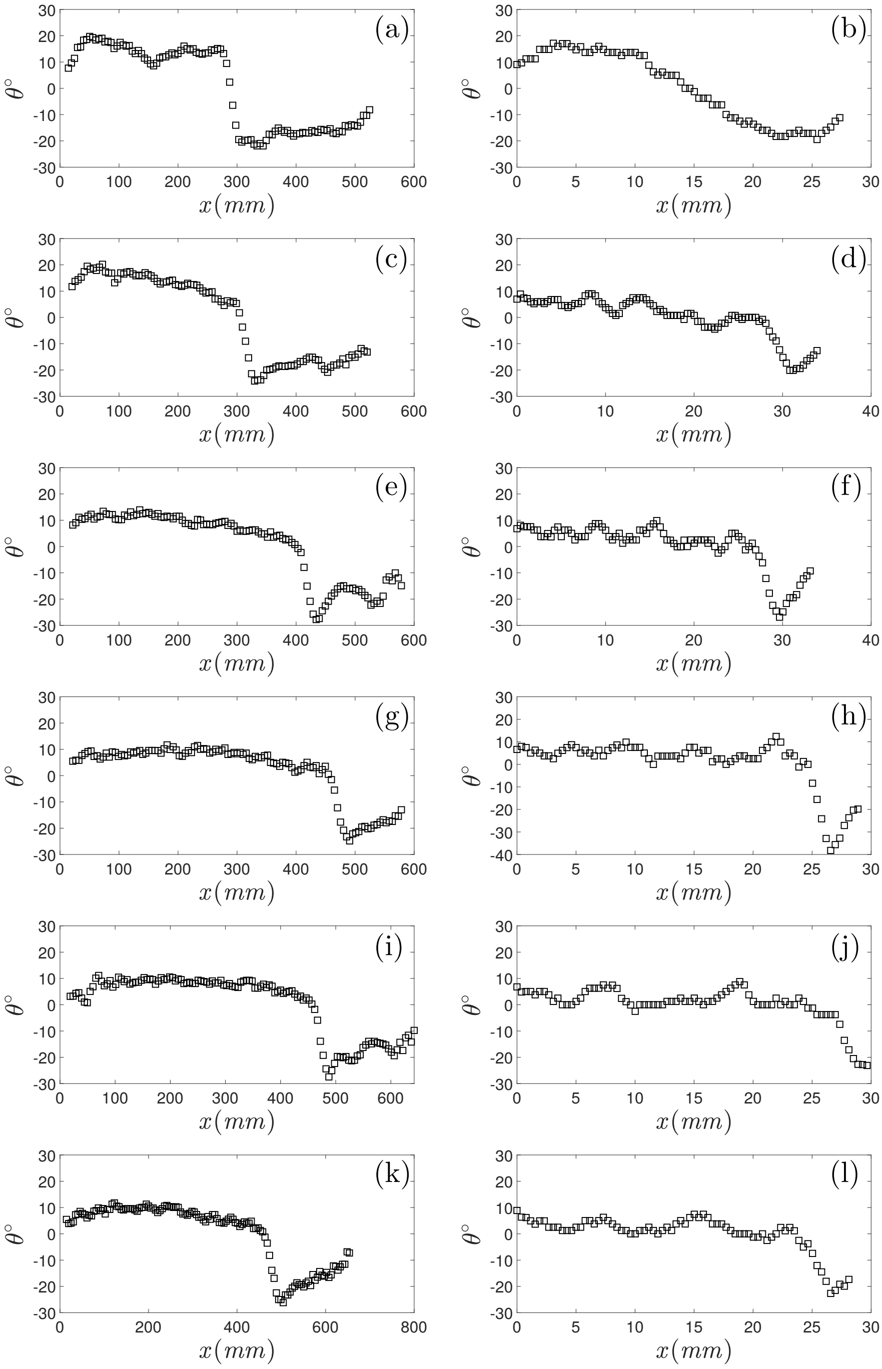

Figure S5. Local slope θ as a function of the longitudinal coordinate x for different time instants for the initial pile being deformed into a dune. Figures (a),(c), (e),(g), (i) and (k) correspond respectively to 4 s, 15 s, 39 s, 64 s, 76 s and 800 s of experiments (Figure 2 of the paper), and Figures (b), (d), (f), (h), (j) and (l) to 0 s, 1 s, 5 s, 7 s, 85 s and 120 s of numerical simulations (Figure 4 of the paper). Figures k and l present a stoss mean value of 8.0° and 3.5° with standard deviations of 2.0° and 2.1°, respectively.

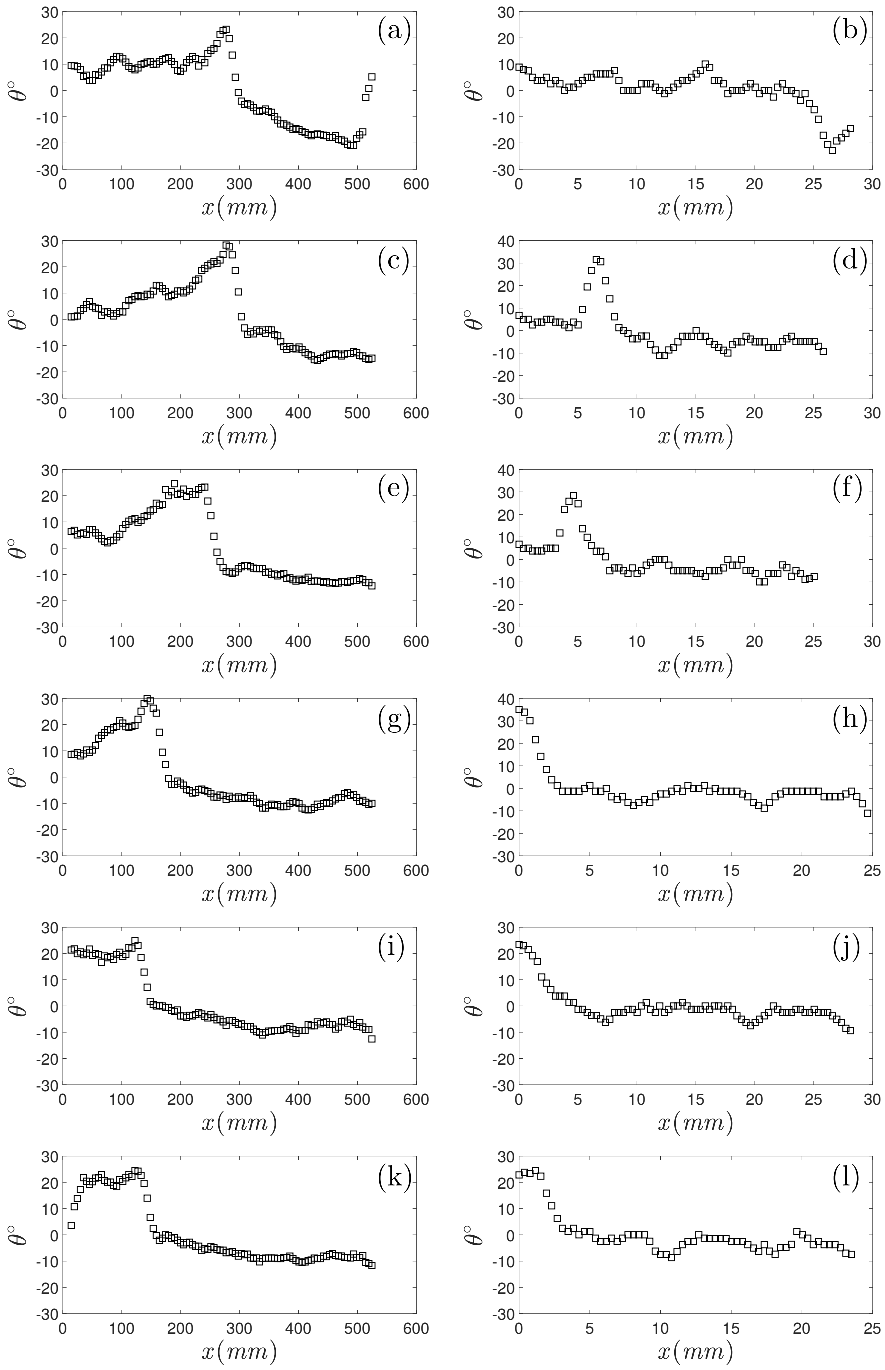

Figure S6. Local slope θ as a function of the longitudinal coordinate x for different time instants for the a dune under a reversed flow. Figures (a),(c), (e),(g), (i) and (k) correspond respectively to 28 s, 43 s, 51 s, 100 s, 315 s and 729 s of experiments (Figure 6 of the paper), and Figures (b), (d), (f), (h), (j) and (l) to 0 s, 1 s, 3 s, 45 s, 75 s and 160s of numerical simulations (Figure 8 of the paper). Figures k and l present a stoss mean value of -7.4° and -3.0° with standard deviations of 2.3° and 2.7°, respectively.

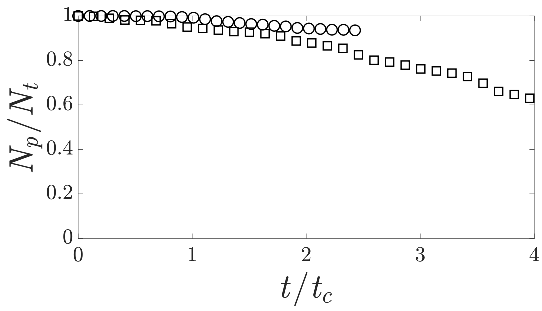

Figure S7. Time evolution of the ratio between the numbers of particles lost by the barchan N_p and the initial number of particles. Circles correspond to a barchan developed from a conical pile and squares to a barchan undergoing flow reversal.

t (s)	N_{mv}	N_t	N_{mv}/N_t
1	573	11261	5.1%
5	220	11015	2.0%
10	135	9415	1.4%
15	12	9104	0.1%
20	153	8815	1.7%
25	30	8587	0.3%
30	3118	8323	37.5%
35	275	7957	3.5%
40	306	7801	3.9%
45	69	7809	0.9%
50	189	7766	2.4%
55	11	7533	0.1%
60	397	7441	5.3%
65	25	7485	0.3%
70	262	7483	3.5%
75	248	7422	3.3%
80	79	7373	1.1%
85	27	7239	0.4%
90	1441	7182	20.1%
95	264	7165	3.7%
100	6	7073	0.1%
105	38	6976	0.5%
110	51	6970	0.7%
115	89	7022	1.3%
120	72	6944	1.0%

Figure S8. Table listing the number of grains moving as bedload in the central slice at each instant, for the initial heap being developed into a barchan dune. In the table, t is the time, N_{mv} is the number of moving grains in the central slice, N_t is the total number of grains in the central slice, and N_{mv}/N_t is the ratio between the two.

t (s)	N_{mv}	N_t	N_{mv}/N_t
1	122	6726	1.8%
5	74	6365	1.2%
10	46	6427	0.7%
15	197	6463	3.0%
20	28	6168	0.5%
25	101	6151	1.6%
30	1212	6144	19.7%
35	66	6076	1.1%
40	39	6103	0.6%
45	26	6091	0.4%
50	5	5959	0.1%
55	92	5910	1.6%
60	0	5935	0.0%
65	85	5933	1.4%
70	16	5917	0.3%
75	174	5991	2.9%
80	376	5951	6.3%
85	8	6020	0.1%
90	64	6011	1.1%
95	49	5935	0.8%
100	8	6017	0.1%
105	121	5845	2.1%
110	4	5855	0.1%
115	0	5848	0.0%
120	6	5805	0.1%
125	1	5882	0.0%
130	6	5810	0.1%
135	95	5649	1.7%
140	46	5612	0.8%
145	806	5545	14.5%
150	63	5692	1.1%
155	666	5477	12.2%
160	270	5421	5.0%
165	29	5328	0.5%
170	1659	5093	32.6%
175	30	4855	0.6%
180	31	4936	0.6%
185	97	4933	2.0%
190	564	4769	11.8%
195	9	4740	0.2%
200	550	4633	11.9%
205	15	4712	0.3%
210	44	4310	1.0%
215	31	4314	0.7%
220	5	4310	0.1%
225	772	4246	18.2%
230	322	4146	7.8%
235	23	3818	0.6%
240	311	3802	8.2%

Figure S9. Table listing the number of grains moving as bedload in the central slice at each instant, for a barchan dune undergoing reversal. In the table, t is the time, N_{mv} is the number of moving grains in the central slice, N_t is the total number of grains in the central slice, and N_{mv}/N_t is the ratio between the two

(a)

(b)

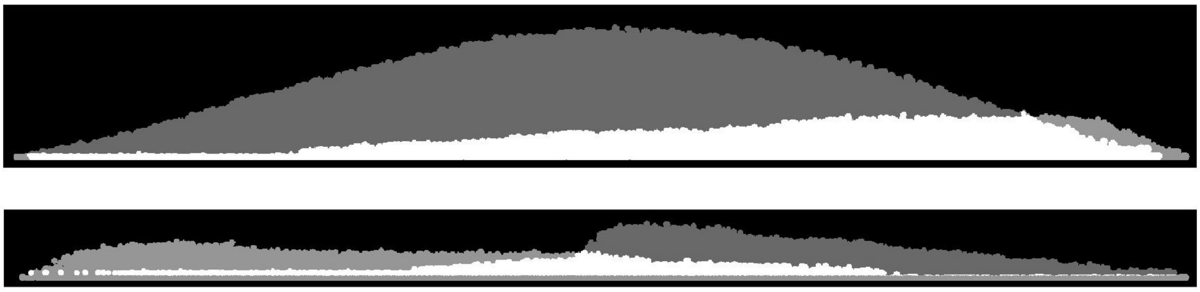

Figure S10. Superposition of the side view for (a) initial conical pile (t = 0 s, in darker gray) and developed (t = 120 s, in lighter gray) bedforms from figure 4 of the main manuscript (intersection appears in white) and (b) reversing flow direction (t = 1 s, in darker gray) and reversed dune (t = 160 s, in lighter gray) bedforms from figure 8 of the main manuscript (intersection appears in white).